# Photoionization of two-electron atoms via highly doubly excited states: Numerical and semiclassical results

Min-Ho Lee, Chang Woo Byun, and Nark Nyul Choi*
*School of Natural Science, Kumoh National Institute of Technology, Gumi, Gyeongbuk 730-701, Korea*

Gregor Tanner
*School of Mathematical Sciences, University of Nottingham, University Park, Nottingham NG7 2RD, United Kingdom*
(Received 19 January 2010; published 27 April 2010)

The quantum regime of highly doubly excited states in two-electron atoms has, so far, been largely inaccessible both to numerical methods as well as to experiments. Recent advances in semiclassical closed orbit theory in combination with a quantum mapping approach have shown a new way into this region of high dynamical complexity. In particular, new scaling laws near the double-ionization threshold as well as the dominant semiclassical contributions to the total photoionization cross section can be identified. We will present this new approach here in all its detail. It is based on representing the photoionization cross section in terms of quantum maps. These quantum maps or quantum propagators are used as a starting point for developing an efficient numerical method for calculating cross sections. Furthermore, by writing the quantum operators in semiclassical approximations, it is possible to interpret the quantum results in terms of classical triple collision orbits and to derive threshold laws near the three-particle breakup point. Semiclassical and numerical quantum results show excellent agreement for a model system, namely collinear helium.

DOI: 10.1103/PhysRevA.81.043419 PACS number(s): 32.80.Fb, 03.65.Sq, 05.45.Mt

## I. INTRODUCTION

Three-body Coulomb systems, in general, and two-electron atoms, in particular, serve as a test bed for our understanding of many-particle quantum dynamics and form an integral part of modern atomic physics. Enormous progress was made toward giving a full quantum description of two-electron atoms over the whole energy range. The bound-state spectrum and the structure of low-lying doubly excited resonances is now well understood, see, for example, Ref. [1] for an overview. Likewise, for energies above the three-particle breakup threshold, very efficient numerical methods are now available such as *exterior complex scaling* [2,3], (see also Ref. [4]), *convergent closed coupling* methods [5,6], or advanced *hyperspherical R-matrix* techniques using semiclassical outgoing waves [7,8]. This makes it possible to give detailed numerical predictions for absolute cross sections from energies above the double-ionization threshold ranging from near the threshold all the way to the high-energy end of the double-ionization continuum. In particular, the strong electron-electron correlation effects near the three-particle breakup threshold can now be reproduced in detail. For example, Wannier's threshold law [9] has recently been confirmed numerically, both for the total cross section [10] as well as for partial cross sections [11] and experimental results near the threshold [12–14] are now in good agreement with theory in all details. Given these successes, the interest in the double-ionization regime has shifted toward the description of two-photon double ionization, see, for example, Ref. [15], as well as multiphoton double ionization in intense and short laser pulses, see Ref. [16].

There is, however, still a considerable gap in our knowledge of the quantum dynamics of two-electron atoms in the energy range of highly doubly excited resonances *below* the double-ionization threshold. The regime of low-lying doubly excited states is governed by approximate quantum numbers, which can be understood in terms of group-theoretical or semiclassical arguments, see Ref. [1]. These classification schemes break down when approaching the double-ionization threshold from below and one enters an energy region that has remained largely unexplored until today.

Recent experimental progress in detector technology and synchrotron sources has made it possible to get fully resolved single-ionization spectra up to $N \approx 15$ both for partial [17–20] and total [21,22] photoionization cross sections. Here, the quantum number $N$ refers to the hydrogen-like state of the remaining ion with energy $I_N = -\frac{Z^2}{2N^2}$ and $Z$ is the charge of the nucleus. Numerical efforts for calculating the photoionization cross section have advanced slowly [23] reaching now up to $N \approx 20$ [22,24] for total cross sections using complex rotation techniques and $N = 9$ [19,25,26] for partial cross sections based on $R$-matrix methods; progress is hampered here by the fast increase in basis size necessary to achieve convergence for increasing $N$ values. The numerical results in Refs. [22–24] clearly show a selective breakdown of labeling individual resonances in terms of approximate quantum numbers; many important questions remain open, however, such as whether approximate symmetries persist when approaching the double-ionization threshold from below.

The rich resonance spectrum for energies $E < 0$ is intricately linked to the complexity of the underlying classical dynamics of this three-body Coulomb problem. The classical dynamics are mostly chaotic in this energy regime, which is reflected in the statistical properties of the resonance spectrum [21,27]. Any regular structure of the quantum spectrum, where it exists, must have a counterpart in the corresponding classical dynamics—but again, only little is known about the phase-space structure of this many-body problem. The dynamics

*nnchoi@kumoh.ac.kr

 

in various two-dimensional subspaces were studied in detail, see Ref. [1]; a global description, which can, for example, explain the existence of approximate quantum numbers from a semiclassical point of view is, however, still in its infancy [28,29]. The chaotic part of the classical dynamics, on the other hand, is dominated by the complex folding patterns of the stable and unstable manifolds of the triple collision, which was analyzed in detail in Refs. [29–32].

A semiclassical description of photoionization cross sections for two-electron atoms taking into account the nature of the triple collision was worked out in Ref. [33] for total cross sections and in Ref. [20] for partial cross sections. In particular, it can be demonstrated that the fluctuations in the total and partial cross sections due to overlapping resonances decays algebraically with an exponent determined by the triple collision singularity *different* from Wannier's exponent. Furthermore, the fluctuations can be described in terms of contributions from closed orbits starting and ending in the triple collision—the so-called *closed triple collision orbits* (CTCO).

The present article provides a detailed derivation of the results given in Ref. [33]. The technique of quantum maps is introduced starting from first principles and the semiclassical treatment is presented in all detail including a derivation of the modified exponent. In addition, we will introduce a numerical technique developed by Mrugała and co-workers [34–36] for calculating photoionization cross sections and present improved numerical calculations of total cross section and scattering wave solutions.

The article is organized as follows: In sec. II, we introduce the half-space scattering problems for an inner and outer region around the core and describe the corresponding Green functions in terms of quantum maps. In sec. III, we present a variant of the *smooth variable discretization* technique (SVD $L$ propagation) and demonstrate the connection to the quantum mapping approach developed in sec. II. A semiclassical version of the quantum map formalism is used in sec. IV to derive a closed orbit formula for two-electron atoms taking into account the singular behavior near the triple collision. It also forms the basis for deriving the modified exponent. Numerical results for a collinear version of the two-electron problem using the SVD $L$-propagation methods are presented in sec. V and compared with the semiclassical predictions.

## II. PHOTOIONIZATION CROSS SECTION IN TERMS OF QUANTUM MAPS

### A. Introduction

We are interested in the photoionization signal for single-electron ionization near the double-ionization threshold. This part of the photoionization cross section is dominated by an increasing number of Rydberg resonances series, which mix more and more strongly as one approaches the threshold. Large parts of the spectrum are still "terra incognito" both from a numerical or analytical as well as from an experimental point of view [1]. We will develop a theoretical framework here, which allows us to give new insight into this energy regime from a semiclassical point of view, as discussed in sec. IV and also forms the building blocks for an efficient, new numerical method as presented in sec. III.

The starting point is the photoionization cross section written in the dipole approximation

$$\sigma(E) = \frac{4\pi^2}{c}\omega \sum_f |\langle \Phi_f^-(E)|D|\phi_0\rangle|^2, \tag{1}$$

where $c$ is the speed of light, $\phi_0$ is the initial-state wave function, $D = \boldsymbol{\pi}(\mathbf{r}_1 + \mathbf{r}_2)$ is the dipole operator with $\boldsymbol{\pi}$, the polarization of the incoming photon, and $\mathbf{r}_i$ is the position of electron $i$. The sum is over all open channels where $\Phi_f^-(E)$ denotes the corresponding final-state scattering wave with incoming boundary conditions at energy $E = E_0 + \omega$ with $\omega$ the photon energy and $E_0$ denotes the energy of the initial state. Note that we work in the infinite nucleus mass approximation, that is, the position of the nucleus is fixed at the origin; furthermore, atomic units are used throughout this article. Considerable effort was devoted to calculating the final-state wave functions $\Phi_f$ (both below and above the three-particle breakup point [1,2,4,11,19,25,26]) in Eq. (1) taking into account the full electron-electron correlation. Below the double-ionization threshold, it is the large number of open channels, the high density of resonance states near the channel thresholds and strong interseries mixing (calling for an increasingly finer energy resolution), which pose enormous challenges for entering the threshold regime from below.

The cross section (1) can also be written in terms of the retarded Green function $G(E)$ of the full three-particle problem, that is, [37,38]

$$\sigma(E) = -\frac{4\pi}{c}\omega \mathrm{Im}\langle D\phi_0|G(E)|D\phi_0\rangle. \tag{2}$$

In the following, we will express the three-body Green function in terms of local scattering matrices or quantum Poincaré maps, which will form the basis of the semiclassical and numerical calculations in Secs. III and IV. For three-body problems, it is convenient to introduce the hyperradius $R = \sqrt{r_1^2 + r_2^2}$, where $r_i$ denotes the distance of electron $i$ from the origin; we furthermore chose a surface of section $\Sigma$ at a fixed hyperradius $R_0$. The main idea is to split the quantum problem into two half-scattering problems and to match the quantum dynamics at the dividing surface $\Sigma$. The quantum Hamiltonian of each half-scattering problem has well-defined scattering channels and associate scattering matrices. The Green function and the cross section in Eq. (2) can then be written in terms of these scattering matrices and the scattering solutions of the half-space Hamiltonians. We present the treatment here for two-electron atoms using hyperspherical coordinates, a general description of the method can be found in Refs. [39,40]. The surface $\Sigma$ naturally leads to a partition of the configuration space into physically distinct regions. In particular, quantum contributions to Eq. (2) from the inner region $R < R_0$ are insensitive to the total energy. Contributions from the outer region test the full scale of the classically allowed region of size $|E|^{-1}$ and will be responsible for the resonance structures near the double-ionization threshold at $E = 0$.

### B. Hyperspherical coordinates

Writing the three-body Hamiltonian in hyperspherical coordinates $R,\mathbf{\Omega} = (\alpha,\hat{\mathbf{r}}_1,\hat{\mathbf{r}}_2)$ with

$$R = \sqrt{r_1^2 + r_2^2}, \quad \alpha = \tan^{-1}\left(\frac{r_2}{r_1}\right), \quad \hat{\mathbf{r}}_i = \frac{\mathbf{r_i}}{r_i}, \tag{3}$$

one obtains

$$\left(-\frac{1}{2}\frac{\partial^2}{\partial R^2} + H_R\right)\Psi = E\Psi, \tag{4}$$

with $\Psi(R,\mathbf{\Omega}) = R^{5/2}\sin(\alpha)\cos(\alpha)\Phi(\mathbf{r}_1,\mathbf{r}_2)$, where $\Phi$ denotes a solution of the Schrödinger equation in Cartesian coordinates. The adiabatic Hamiltonian $H_R$ with

$$H_R = \frac{1}{2}\frac{\Lambda^2}{R^2} + \frac{1}{R}V(\mathbf{\Omega}), \tag{5}$$

depends parametrically on the hyperradius $R$ with the "grand angular momentum"—operator $\Lambda$ defined as

$$\Lambda^2 = \left(-\frac{\partial^2}{\partial\alpha^2} + \frac{\mathbf{l}_1^2}{\cos^2\alpha} + \frac{\mathbf{l}_2^2}{\sin^2\alpha}\right) - \frac{1}{4},$$

which is the angular momentum operator in six dimensions [41,42]. Here, $\mathbf{l}_i$ denotes the three-dimensional (3D) angular momentum operator for electron $i$ and $V(\mathbf{\Omega})/R$ is the three-body Coulomb potential written in hyperspherical coordinates with

$$V(\mathbf{\Omega}) = -\frac{Z}{\cos\alpha} - \frac{Z}{\sin\alpha} + \frac{1}{\sqrt{1 - \hat{\mathbf{r}}_1\cdots\hat{\mathbf{r}}_2\sin 2\alpha}}. \tag{6}$$

The adiabatic Hamiltonian (5) acts on the angle variables $\mathbf{\Omega}$ alone and has a discrete spectrum, that is,

$$H_R\psi_n(\mathbf{\Omega};R) = U_n(R)\psi_n(\mathbf{\Omega};R), \tag{7}$$

with eigenfunctions $\psi_n$ and eigenvalues $U_n$ depending parametrically on $R$. This property is essential for the treatment described in the following. Due to the reality of the potentials, we can choose the $\psi_n$'s to be orthonormalized real functions (which will be assumed from now on).

### C. The half-space scattering problems

In the following, we will present a scattering formulation of the Green function. This method was originally developed in a semiclassical context by Bogomolny [43] and Doron and Smilansky [44]; a formulation in terms of quantum operators or quantum maps was given in Refs. [39,40]. We will present here a derivation tailored to the calculation of the photoionization cross section in two-electron atoms. A similar approach was adopted in Refs. [33,45] differing, however, in the treatment of closed channels.

First, we consider the half-scattering problem with Hamiltonian $H_0$ defined as

$$H_0 = -\frac{1}{2}\frac{\partial^2}{\partial R^2} + \begin{cases} H_R & \text{for} \quad R < R_0 \\ H_{R_0} & \text{for} \quad R > R_0 \end{cases}, \tag{8}$$

where the dividing surface $\Sigma$ at hyperradius $R = R_0$ is chosen to be of the size of the initial-state wave function $\phi_0$. The solutions of the corresponding Schrödinger equation at fixed energy $E$ can be written in the form of outgoing $|\Psi_n^+\rangle$ and incoming $|\Psi_n^-\rangle$ scattering waves, which for $R > R_0$ take on the form

$$\Psi_n^+(R,\mathbf{\Omega}) = \frac{1}{\sqrt{2\pi}}\left[\frac{1}{\sqrt{k_n}}\psi_n(\mathbf{\Omega};R_0)e^{-ik_n(R-R_0)} + \sum_l s_{ln}\frac{1}{\sqrt{k_l}}\psi_l(\mathbf{\Omega};R_0)e^{ik_l(R-R_0)}\right], \tag{9}$$

$$\Psi_n^-(R,\mathbf{\Omega}) = \frac{1}{\sqrt{2\pi}}\left[\frac{1}{\sqrt{k_n^*}}\psi_n(\mathbf{\Omega};R_0)e^{ik_n^*(R-R_0)} + \sum_l s_{ln}^\dagger\frac{1}{\sqrt{k_l^*}}\psi_l(\mathbf{\Omega};R_0)e^{-ik_l^*(R-R_0)}\right]. \tag{10}$$

Here, $k_n = \sqrt{E - U_n(R_0)}$ is the channel wave number and $\mathbf{s}$ represents the scattering matrix for the half-scattering problem, see Fig. 1. Note, that the sums in Eqs. (9) and (10) are taken over both open $[E \geqslant U_n(R_0)]$ and closed $[E < U_n(R_0)]$ channels, where the latter are characterized by an imaginary wave number $k_n = i\kappa_n = i\sqrt{U_n(R_0) - E}$. (The notion of an "outgoing" or "incoming" closed channel is a bit obscure here and is justified only by comparison with the corresponding open channels). The wave functions correspond to energy-normalized states. Note that we have

$$|\mathbf{\Psi}^+\rangle = |\mathbf{\Psi}^-\rangle^* = \langle\mathbf{\Psi}^-|^T, \tag{11}$$

both for open and closed wave vector components $|\Psi_n\rangle$, which follows from the symmetry of the Green function and the scattering matrix for real potentials [39,40], that is,

$$G_0^T = G_0, \quad \mathbf{s} = \mathbf{s}^T, \tag{12}$$

where $T$ denotes the transpose of an operator or matrix.

The retarded Green function $G_0$ of the half-scattering problem is defined as the solution of

$$(E - H_0)\,G_0 = \delta(R - R')\delta(\mathbf{\Omega} - \mathbf{\Omega}'), \tag{13}$$

with outgoing boundary conditions; that is, the Green function can be written as a superposition of outgoing waves (with respect to the coordinate $R$) for $R \to \infty$. In particular, for source points $R' < R_0$, one obtains for $R > R_0$,

$$G_0(R,\mathbf{\Omega};R',\mathbf{\Omega}') = \frac{1}{\sqrt{2\pi}}\sum_n a_n\frac{1}{\sqrt{k_n}}\psi_n(\mathbf{\Omega};R_0)e^{ik_n(R-R_0)}, \tag{14}$$

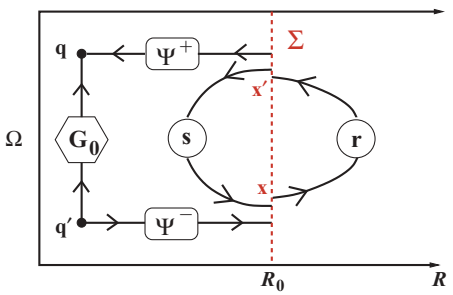


FIG. 1. (Color online) Schematic representation of the Green function, Eq. (20) in terms of the local scattering operators $\mathbf{s}$ and $\mathbf{r}$ and the local scattering solutions $\mathbf{\Psi}^\pm$; note, $\mathbf{q} \equiv (\mathbf{r}_1,\mathbf{r}_2)$ here.

with coefficients $a_n = a_n(R',\mathbf{\Omega}')$ depending on the source point $(R',\mathbf{\Omega}')$. One can show, using Eq. (12) that the $a_n$'s are given as

$$a_n(R',\mathbf{\Omega}') = -2\pi i \Psi_n^+(R',\mathbf{\Omega}'), \tag{15}$$

see Appendix A for details.

Defining an associate half-scattering problem with Hamiltonian $H_1$

$$H_1 = -\frac{1}{2}\frac{\partial^2}{\partial R^2} + \begin{cases} H_{R_0} & \text{for} \quad R < R_0 \\ H_R & \text{for} \quad R > R_0 \end{cases}, \tag{16}$$

one obtains scattering solutions equivalent to Eqs. (9) and (10), which in turn define an outward scattering or reflection matrix $\mathbf{r}$. Its matrix elements $r_{ln}$ express the fraction of a wave solution passing through $\Sigma$ from the region $R < R_0$ with channel number $n$ and returning to $\Sigma$ with channel number $l$ due to reflection in the outer interaction region $R > R_0$.

### D. The Green function

We can now formulate the full Green function (2) in terms of the local scattering or reflection matrices $\mathbf{s}$ and $\mathbf{r}$ and the half-scattering wave solutions $|\Psi_n^\pm\rangle$ as defined in the last section. The dividing surface $\Sigma$ is chosen such that the initial wave function $\phi_0$ entering the matrix element (2) is localized in the region $R < R_0$; we can thus focus on the behavior of the Green function $G(R,\mathbf{\Omega};R',\mathbf{\Omega}')$ in the region $R, R' < R_0$. It has the form

$$G(R,\mathbf{\Omega};R',\mathbf{\Omega}') = \sum_n c_n^+ \Psi_n^+(R,\mathbf{\Omega}) + G_0(R,\mathbf{\Omega};R',\mathbf{\Omega}'), \tag{17}$$

where $G_0$ is the retarded Green function of the half-scattering problem, Eq. (8), and the $|\Psi_n^+\rangle$ are the scattering solutions introduced in Eq. (9) continued into the region $R < R_0$. The coefficients $c_n^+$ depend on the source point $(R',\mathbf{\Omega}')$ as well as on the full, correlated three-particle dynamics for $R > R_0$.

To determine the coefficients $c_n$, we note that the outgoing part of the wave solution (17) directly at the surface of section $\Sigma$ is given as

$$G_{\text{out}}(R_0,\mathbf{\Omega},R',\mathbf{\Omega}') = \frac{1}{\sqrt{2\pi}}\sum_n \left[ a_n \frac{1}{\sqrt{k_n}}\psi_n(\mathbf{\Omega};R_0) + \sum_l \frac{1}{\sqrt{k_l}}\psi_l(\mathbf{\Omega};R_0) s_{ln} c_n^+ \right],$$

where the first term stems from the Green function $G_0$ and the second part is due to the outgoing part of the homogeneous scattering solution $\Psi_n^+$. Similarly, the incoming wave part at $\Sigma$ is given as

$$G_{\text{in}}(R_0,\mathbf{\Omega},R',\mathbf{\Omega}') = \frac{1}{\sqrt{2\pi}}\sum_n c_n^+ \frac{1}{\sqrt{k_n}}\psi_n(\mathbf{\Omega};R_0).$$

To obtain a stationary solution, we must ensure that the part of the outgoing wave solution $G_{\text{out}}$, which is reflected back to the region $R < R_0$ via the reflection matrix $\mathbf{r}$ coincides with the incoming wave $G_{\text{in}}$. This leads to a consistency equation for the coefficients of the form

$$\mathbf{c}^+ = \mathbf{r}\mathbf{s}\mathbf{c}^+ + \mathbf{r}\mathbf{a},$$

or

$$\mathbf{c}^+ = (1 - \mathbf{r}\mathbf{s})^{-1}\mathbf{r}\mathbf{a}, \tag{18}$$

where $\mathbf{c}^+$ and $\mathbf{a}$ denote the vectors of coefficients taken over all channel numbers. Making use of Eq. (15), one finally obtains

$$G(R,\mathbf{\Omega};R',\mathbf{\Omega}') = G_0(R,\mathbf{\Omega};R',\mathbf{\Omega}') - 2\pi i \Psi^+(R,\mathbf{\Omega}) \times [\mathbf{1} - \mathbf{r}\mathbf{s}]^{-1}\mathbf{r}\Psi^+(R',\mathbf{\Omega}'), \tag{19}$$

or using the relation (11)

$$G(E) = G_0(E) - 2\pi i |\Psi^+(E)\rangle [\mathbf{1} - \mathbf{r}(E)\mathbf{s}(E)]^{-1} \times \mathbf{r}(E)\langle\Psi^-(E)|. \tag{20}$$

We may interpret the scattering matrices $\mathbf{s}$, $\mathbf{r}$ as quantum maps mapping wave functions from $\Sigma$ back onto $\Sigma$, see Fig. 1. Here, $\mathbf{s}$ takes care of wave solutions being reflected in the interior region $R < R_0$ whereas $\mathbf{r}$ describes waves radiating out from $\Sigma$ into the region $R > R_0$ and returning to $\Sigma$. Likewise, we may view $\langle\Psi^-|$, $|\Psi^+\rangle$ as quantum maps, projecting wave functions from the interior onto the section $\Sigma$ as well as mapping boundary function from $\Sigma$ into the region $R < R_0$, respectively. For a schematic view of the transformations forming the Green function in Eq. (20), see Fig. 1. The contributions from $G_0$ may be considered as a smooth background part.

### E. The photoionization cross section

We make use of the general relation connecting the imaginary part of the Green function to the open channel scattering solutions, see Eqs. (1) and (2), that is,

$$\text{Im}G_0 = -\pi \sum_{n\in\text{open}} |\Psi_n^\pm\rangle\langle\Psi_n^\pm|,$$

where the summation is here only over all the *open* channels. After setting

$$\mathbf{d} = \langle\Psi^+|D|\phi_0\rangle = \langle\phi_0|D|\Psi^-\rangle, \tag{21}$$

where we use that both $\phi_0$ and $D$ are real functions and inserting Eq. (20) into Eq. (2), we obtain for the total photoionization cross section

$$\sigma(E) = \sigma_0 + \sigma_{\text{fl}} = \frac{4\pi^2}{c}\omega[\mathbf{d}_o^\dagger\mathbf{d}_o + 2\text{Re}\mathbf{d}^\dagger(\mathbf{1} - \mathbf{r}\mathbf{s})^{-1}\mathbf{r}\mathbf{d}^*]. \tag{22}$$

Here, $\mathbf{d}_o$ denotes the components of $\mathbf{d}$ corresponding to open channels. Note that Eq. (22) is an approximation in so far as it neglects contributions from the initial wave function lying outside $R_0$. This contribution can be made arbitrarily small by increasing $R_0$.

One may identify the contribution $\mathbf{d}_o^\dagger\mathbf{d}_o$ as a "smooth background signal" $\sigma_0$, whereas the information about resonances is (mostly) contained in $\sigma_{\text{fl}}$. This part gives rise to a "fluctuating signal" in the regime of strongly overlapping resonances, which will be discussed in sec. V C, see also Fig. 6. Equation (22) is the main result of this section. We stress, that both open and closed channels contribute to $\sigma_{\text{fl}}$; our formula

(22) reproduces previously published results by Granger and Greene [45] when neglecting the contributions from closed channels, see Appendix B, but is more general otherwise. The open channel formulation given explicitly for the first time in Ref. [45] was used earlier in Refs. [46–49] to model core scattering or quantum defect effects in a semiclassical treatment. It was also the starting point of the semiclassical analysis in Ref. [33], which uncovered the scaling laws in the photoionization cross section of two-electron atoms discussed in more detail in sec. IV.

## III. NUMERICAL APPROACHES FOR HIGHLY EXCITED STATES IN TWO-ELECTRON SYSTEMS

### A. The generalized log-derivative propagator

The scattering matrices **s** and **r** in Eq. (22) can be obtained by solving the Schrödinger equation (4) with Hamiltonians (8) and (16), respectively. The wave function $\Psi(R,\mathbf{\Omega})$ can be expanded in the adiabatic basis consisting of the eigenfunctions $\psi_n(\mathbf{\Omega};R)$ defined in Eq. (7), such as

$$\Psi(R,\mathbf{\Omega}) = \sum_n F_n(R)\psi_n(\mathbf{\Omega};R); \tag{23}$$

the sum over $n$ is here again taken both over open and closed channels. Substitution of this expansion into the Schrödinger equation produces a set of coupled-channel equations [41]

$$\left(\frac{d^2}{dR^2} + 2[E - U_n(R)]\right) F_n(R) + \sum_m \left[2A_{nm}(R)\frac{d}{dR} + C_{nm}(R)\right] F_m(R) = 0, \tag{24}$$

where $A$ and $C$ are the nonadiabatic coupling matrices

$$A_{nm}(R) = \langle\psi_n(\mathbf{\Omega};R)|\frac{\partial}{\partial R}\psi_m(\mathbf{\Omega};R)\rangle_\Omega, \tag{25}$$

$$C_{nm}(R) = \langle\psi_n(\mathbf{\Omega};R)|\frac{\partial^2}{\partial R^2}\psi_m(\mathbf{\Omega};R)\rangle_\Omega, \tag{26}$$

and $\langle\cdots\rangle_\Omega$ denotes integration over $\mathbf{\Omega}$.

A typical problem in finding numerical solutions of the coupled-channel equations is the instabilities introduced through closed channels. As one propagates into the classically forbidden regime, the radial functions **F**, where $\mathbf{F}(R)$ denotes the column vector with components $F_n(R)$, grow exponentially for closed-channel components. These contributions soon dominate the whole system of equations leading to numerical instabilities. In the log-derivative method devised by Johnson [50] the stability problem is eliminated by propagating a log-derivative matrix directly rather than the wave function and its derivative. However, the method is restricted to inelastic scattering problems, that is, the calculation of reflection amplitudes. Introducing an invariant embedding type propagator, Mrugała and Secrest [34] generalized the method making it possible to also handle any reactive (transmission) amplitudes. They defined a generalized log-derivative propagator, called $L$ propagator in what follows, in an interval $[R',R'']$ in the form of a $2M \times 2M$ block matrix

$$\mathcal{L}(R',R'') = \begin{pmatrix} \mathcal{L}^{(1)}(R',R'') & \mathcal{L}^{(2)}(R',R'') \\ \mathcal{L}^{(3)}(R',R'') & \mathcal{L}^{(4)}(R',R'') \end{pmatrix}. \tag{27}$$

It connects **F**, the solutions of Eq. (24), and its derivative $\mathbf{F}'$ at the start and end points of the propagation $R'$ and $R''$, that is,

$$\begin{pmatrix} \mathbf{F}'(R') \\ \mathbf{F}'(R'') \end{pmatrix} = \mathcal{L}(R',R'') \begin{pmatrix} \mathbf{F}(R') \\ \mathbf{F}(R'') \end{pmatrix}; \tag{28}$$

here, $M$ is the total number of channels included in the calculation. Noting that

$$\langle\boldsymbol{\psi}(\mathbf{\Omega};R)|\frac{\partial}{\partial R}\Psi(R,\mathbf{\Omega})\rangle_\Omega = \mathbf{F}'(R) + \mathbf{A}(R)\mathbf{F}(R), \tag{29}$$

it is more convenient to introduce [35]

$$\mathbf{L}(R',R'') = \begin{pmatrix} \mathbf{L}^{(1)}(R',R'') & \mathcal{L}^{(2)}(R',R'') \\ \mathcal{L}^{(3)}(R',R'') & \mathbf{L}^{(4)}(R',R'') \end{pmatrix}, \tag{30}$$

where

$$\mathbf{L}^{(1)}(R',R'') = \mathcal{L}^{(1)}(R',R'') + \mathbf{A}(R'), \tag{31}$$

$$\mathbf{L}^{(4)}(R',R'') = \mathcal{L}^{(4)}(R',R'') + \mathbf{A}(R''). \tag{32}$$

Equation (28) can now be rewritten as

$$\begin{pmatrix} \langle\boldsymbol{\psi}(\mathbf{\Omega};R')|\partial\Psi(R',\mathbf{\Omega})/\partial R'\rangle_\Omega \\ \langle\boldsymbol{\psi}(\mathbf{\Omega};R'')|\partial\Psi(R'',\mathbf{\Omega})/\partial R''\rangle_\Omega \end{pmatrix} = \mathbf{L}(R',R'') \begin{pmatrix} \mathbf{F}(R') \\ \mathbf{F}(R'') \end{pmatrix}. \tag{33}$$

So far, we have not specified how to obtain $\mathcal{L}$ or **L**; we will give details on the numerical procedure in Appendix C. In the following, we will outline the connection between the log-derivative matrix **L** and the scattering matrices **r** and **s** entering the formula for the cross section, Eq. (22). The boundary conditions for the the half-scattering problem related to the Hamiltonian $H_1$ in Eq. (16), which defines the local scattering matrix **r** are

$$\Psi_n(R,\mathbf{\Omega}) = \frac{1}{\sqrt{2\pi}}\left[\frac{1}{\sqrt{k_n}}\psi_n(\mathbf{\Omega};R_0)e^{ik_n(R-R_0)} + \sum_l \frac{1}{\sqrt{k_l}}\psi_l(\mathbf{\Omega};R_0)e^{-ik_l(R-R_0)}r_{ln}\right] \text{for } R \leqslant R_0, \tag{34}$$

with $k_n = \sqrt{E - U_n(R_0)}$. In addition, we introduce a new quantum operator **t**, which maps a solution from $R = R_0$ to $R \to \infty$ with asymptotic form

$$\Psi_n(R,\mathbf{\Omega}) \to \frac{1}{\sqrt{2\pi}}\sum_l \frac{1}{\sqrt{k_l^\infty}}\psi_l(\mathbf{\Omega};R)e^{i\{k_l^\infty R + (Z-1)\ln R/k_l^\infty\}}t_{ln} \quad \text{as} \quad R \to \infty, \tag{35}$$

with $k_n^\infty = \sqrt{E - U_n(\infty)}$; the sum is here only over open channels $l$ at $R \to \infty$. The procedure for evaluating the local scattering matrix **r** consists of finding the propagator $\mathbf{L}(R_0,R_\infty)$ for sufficiently large $R_\infty$ for the outer Hamiltonian system $H_1$, Eq. (16). After substituting Eqs. (34) and (35) into Eq. (33), we can obtain the matrices **r** and **t** such as

$$\begin{pmatrix} \mathbf{r} \\ \mathbf{t} \end{pmatrix} = \begin{pmatrix} \mathbf{L}^{(1)}(R_0,R_\infty)\mathbf{g}(R_0) - \mathbf{g}'(R_0) & \mathbf{L}^{(2)}(R_0,R_\infty)\mathbf{f}^{\mathbf{C}}(R_\infty) \\ \mathbf{L}^{(3)}(R_0,R_\infty)\mathbf{g}(R_0) & \mathbf{L}^{(4)}(R_0,R_\infty)\mathbf{f}^{\mathbf{C}}(R_\infty) - \mathbf{f}^{\mathbf{C}\prime}(R_\infty) \end{pmatrix}^{-1} \begin{pmatrix} \mathbf{f}'(R_0) - \mathbf{L}^{(1)}(R_0,R_\infty)\mathbf{f}(R_0) \\ -\mathbf{L}^{(3)}(R_0,R_\infty)\mathbf{f}(R_0) \end{pmatrix}, \tag{36}$$

where $\mathbf{f}$, $\mathbf{g}$, and $\mathbf{f}^{\mathbf{C}}$ are $M \times M$ diagonal matrices with diagonal elements

$$f_n(R) = \frac{1}{\sqrt{k_n}} e^{ik_n(R-R_0)}, \quad g_n(R) = \frac{1}{\sqrt{k_n}} e^{-ik_n(R-R_0)}, \\ f_n^C(R) = \frac{1}{\sqrt{k_n^\infty}} e^{i\{k_n^\infty R + (Z-1)\ln R/k_n^\infty\}}. \tag{37}$$

The solution relevant to the local scattering matrix $\mathbf{s}$ is $\mathbf{\Psi}^+$, which satisfies the boundary condition (9). By the definition of the wave function $\Psi$ in Eq. (4), the regular solution $\mathbf{\Psi}^+$ should satisfy an additional boundary condition, $\mathbf{\Psi}^+(0) = \mathbf{0}$. Thus we need only $\mathbf{L}^{(4)}(0,R_0)$ to obtain the wave function and its derivative at $R = R_0$. It is easily seen that the local scattering matrix $\mathbf{s}$ can be obtained from $\mathbf{L}^{(4)}(0,R_0)$ such as

$$\mathbf{s} = [\mathbf{f}'(R_0) - \mathbf{L}^{(4)}(0,R_0)\mathbf{f}(R_0)]^{-1}[\mathbf{L}^{(4)}(0,R_0)\mathbf{g}(R_0) - \mathbf{g}'(R_0)]. \tag{38}$$

This concludes our introductory remarks concerning log-derivative propagators and their connection to local scattering matrices of the half-scattering problems. Details on how to calculate $\mathbf{L}$ will be given in Appendix C. In the remainder of this section, we will discuss a transformation technique that leads to an improved method for calculating the log-derivative propagator having better stability properties.

### B. The quasi adiabatic procedure

From a numerical point of view, it is easier to solve the Schrödinger equation by using a diabatic basis set that diagonalizes the kinetic energy operator rather than using an adiabatic one which diagonalizes the potential energy. A change from the adiabatic basis set $\boldsymbol{\psi}(\mathbf{\Omega};R)$ to a diabatic basis $\boldsymbol{\psi}_{\bar{R}}(\mathbf{\Omega}) \equiv \boldsymbol{\psi}(\mathbf{\Omega};\bar{R})$ can be performed by a transformation $\mathbf{T}(R,\bar{R})$, which satisfies the differential equation [51]

$$\left[\mathbf{I}\frac{d}{dR} + \mathbf{A}(R)\right]\mathbf{T}(R,\bar{R}) = 0, \tag{39}$$

with initial condition $\mathbf{T}(\bar{R},\bar{R}) = \mathbf{I}$ at an arbitrarily chosen point $\bar{R}$ such that

$$\boldsymbol{\psi}_{\bar{R}}(\mathbf{\Omega}) = \mathbf{T}^T(R,\bar{R})\boldsymbol{\psi}(\mathbf{\Omega};R). \tag{40}$$

Here $\mathbf{I}$ is the $M \times M$ identity matrix. Then the Schrödinger equation for the transformed radial functions

$$\mathbf{F}_{\bar{R}}(R) = \mathbf{T}^T(R,\bar{R})\mathbf{F}(R), \tag{41}$$

is written as

$$\frac{d^2}{dR^2}\mathbf{F}_{\bar{R}}(R) + \mathbf{w}_{\bar{R}}(R)\mathbf{F}_{\bar{R}}(R) = 0, \tag{42}$$

where $\mathbf{w}_{\bar{R}}(R)$ is the coupling matrix

$$\mathbf{w}_{\bar{R}}(R) = 2\mathbf{T}^T(R,\bar{R})[E\mathbf{I} - \mathbf{U}(R)]\mathbf{T}(R,\bar{R}), \tag{43}$$

and $\mathbf{U}(R)$ is a diagonal matrix with entries given by the eigenvalues $U_n(R)$ defined in Eq. (7). Using the $L$ propagator for these diabatically coupled equations

$$\begin{pmatrix} \mathbf{F}'_{\bar{R}}(R') \\ \mathbf{F}'_{\bar{R}}(R'') \end{pmatrix} = \mathbf{L}_{\bar{R}}(R',R'') \begin{pmatrix} \mathbf{F}_{\bar{R}}(R') \\ \mathbf{F}_{\bar{R}}(R'') \end{pmatrix}, \tag{44}$$

the propagator $\mathbf{L}(R',R'')$ in Eq. (33) can be expressed in the form [35]

$$\mathbf{L}(R',R'') = \begin{pmatrix} \mathbf{T}(R',\bar{R}) & 0 \\ 0 & \mathbf{T}(R'',\bar{R}) \end{pmatrix} \mathbf{L}_{\bar{R}}(R',R'') \times \begin{pmatrix} \mathbf{T}^T(R',\bar{R}) & 0 \\ 0 & \mathbf{T}^T(R'',\bar{R}) \end{pmatrix}. \tag{45}$$

An efficient algorithm for numerically calculating $\mathbf{L}_{\bar{R}}(R',R'')$ was presented in Refs. [34,35] and will be explained in Appendix C1. However, to obtain $\mathbf{T}$, we still need to deal with the differential equation (39), which contains the nonadiabatic coupling matrix $\mathbf{A}$.

### C. The SVD generalized log-derivative method

The difficulties in explicitly calculating the nonadiabatic coupling terms are well known [41,52,53]. They prevent the coupled-channel equations (24) from being of practical use beyond the adiabatic approximation, in which the nonadiabatic couplings are neglected. The nonadiabatic couplings display very sharp changes near narrowly avoided crossings. Accordingly each radial function $F_n(R)$ also changes rapidly following the behavior of the nonadiabatic couplings. Tolstikhin and co-workers [53] observed, however, that the wave function $\Psi(R,\mathbf{\Omega})$ varies slowly as a function of the adiabatic variable $R$ at those points. And this leads to the introduction of a novel approach, the so-called smooth variable discretization (SVD). The main assumption of the SVD is that for a given energy $E$ and a given, yet arbitrary radius $R = \bar{R}$, there is a finite set of adiabatic channel functions $\{\psi_n(\mathbf{\Omega};\bar{R}), n = 1,\ldots,M\}$, which can be regarded as a complete set not only at the radius $\bar{R}$, but also for a finite interval $[R',R'']$ around $\bar{R}$, that is,

$$\sum_l \langle\psi_n(\mathbf{\Omega};R)|\psi_l(\mathbf{\Omega};\bar{R})\rangle_\Omega \langle\psi_l(\mathbf{\Omega};\bar{R})|\psi_m(\mathbf{\Omega};R)\rangle_\Omega = \delta_{nm} \text{for } R \in [R',R'']. \tag{46}$$

Combined with variational methods (such as the $R$-matrix method and the discrete-variable representation) or direct integration methods (such as the renormalized Numerov method), the SVD approach was applied successfully to several few-body problems, proving its efficiency and accuracy and validating the underlying assumptions [53,54].

In the SVD approximation (46), it can be easily seen that the overlap matrix

$$O_{nm}(R,\bar{R}) = \langle \psi_n(\mathbf{\Omega};R)|\psi_m(\mathbf{\Omega};\bar{R})\rangle_\Omega , \tag{47}$$

is actually the solution of the differential equation (39). Thus we can rewrite the relation (45) in the form

$$\mathbf{L}(R',R'') = \begin{pmatrix} \mathbf{O}(R',\bar{R}) & 0 \\ 0 & \mathbf{O}(R'',\bar{R}) \end{pmatrix} \mathbf{L}_{\bar{R}}(R',R'') \times \begin{pmatrix} \mathbf{O}^T(R',\bar{R}) & 0 \\ 0 & \mathbf{O}^T(R'',\bar{R}) \end{pmatrix}. \tag{48}$$

Comparing Eq. (48) with Eq. (45), one observes that the overlap matrix $\mathbf{O}$ replaces the transformation matrix $\mathbf{T}$ and thus removes the first-derivative coupling matrix $\mathbf{A}$ from the coupled equation (24). Difficulties in treating the differential equation involving the nonadiabatic coupling matrix $\mathbf{A}(R)$ are thus circumvented in the SVD approximation.

The size of the interval around a fixed $R = \bar{R}$ in which the SVD approximation is valid is generally much smaller than the range over which the coupled-channel equations are integrated. Thus the SVD $L$-propagation method (48) involves two steps: (i) dividing the range of integration into small sectors and carrying out the numerical computation of the propagator for each sector and (ii) propagating the solution from sector to sector thus accumulating the propagator for the entire integration range $[R',R'']$.

In using the relation (45) the entire range of integration is also divided into small sectors and the diabatic basis set for each sector is chosen at the midpoint of the sector. Thus the above-mentioned two steps are carried out in the $L$-propagation method as in the SVD $L$-propagation method. This means that algorithms for computation of the $L$ propagator $\mathbf{L}(R',R'')$ based on the relation (48) can be easily constructed by using the well-established algorithms [35,36] based on the relation (45) with Eq. (39): One only needs to replace the $\mathbf{T}$'s with $\mathbf{O}$'s throughout.

Details of the SVD-type algorithm for evaluating the propagator $\mathbf{L}(R',R'')$ are given in Appendix C 1. Furthermore, algorithms for the computation of the local scattering wave function $\mathbf{\Psi}^+$ and the initial bound state are given in the rest of Appendix C; these are needed to evaluate the atomic dipole vector $\mathbf{d}$ in Eq. (21).

Before giving the numerical results obtained using the log-derivative method in Sec. V, we will discuss a semiclassical treatment of the total photoionization cross section for two-electron atoms in the next section.

## IV. CLOSED ORBIT THEORY NEAR THE TRIPLE COLLISION—A SEMICLASSICAL TREATMENT

### A. Background

A semiclassical description of the photoionization cross section, Eq. (1), for atomic systems with an underlying chaotic classical dynamics was first developed in Refs. [37,38]. Starting from Eq. (2) and expressing the Green function semiclassically in terms of classical trajectories, resonance-induced fluctuations in the cross section of hydrogen-like atoms in external fields were analyzed. In the semiclassical limit, the support of the wave function $\phi_0$ shrinks to zero relative to the size of the system reducing the integration in Eq. (2) to an evaluation of the Green function at the origin. The relevant contributions to the Green function are then given by classical trajectories starting and ending at the origin giving rise to the name *closed orbit theory* (COT).

The semiclassical theory is valid only for interaction potentials sufficiently smooth at the origin such as hydrogen-like atoms. (The Coulomb singularity can be regularized here and does not pose difficulties). To circumvent the singular behavior due to many-body collisions in few-electron atoms, single-electron excitation in such systems is often treated in quantum defect approximation. These core effects can be modeled semiclassically by introducing diffractive scattering at the central singularity [46,47] or by employing smoothed model potentials near the origin [55].

Such a treatment is not possible when calculating doubly excited states in, for example, two-electron atoms. Both electrons need to be treated on an equal footing here, and the full three-body dynamics near the origin needs to be taken into account semiclassically. The classical dynamics near the origin is dominated by the nonregularizable triple collision singularity. Reducing the integration over the initial state in Eq. (2) to a summation over closed orbits in a semiclassical treatment—the standard approach in COT—cannot be adopted here. The semiclassical contributions to the Green function element in Eq. (2) are given by trajectories with initial and final conditions closer and closer to the triple collision. This leads to diverging stability properties of these orbits becoming infinitely unstable as one approaches the singularity. In the following we will describe our modified COT treatment, which accounts for the instability of the triple collision dynamics.

We note that COT was applied previously to He analyzing experimental photoabsorption spectra with and without external fields [46,56,57]. The part of the spectrum considered in these articles belong to highly asymmetric states where one electron is much more excited than the other. This makes it possible to treat the system in a single-electron approximation and the triple collision dynamics do not play a prominent role. This is different when considering the resonance spectrum as a whole including highly doubly excited states. In the semiclassical limit (which corresponds to $E \to 0$ here), the dominant semiclassical contributions are indeed given by triple collision orbits, as will be shown later in this section.

Before developing the semiclassical theory, we will briefly review some of the properties of the classical dynamics of two-electron atoms.

### B. The classical three-body Coulomb dynamics and closed triple collision orbits

#### *1. Overview and the collinear eZe space*

To carry out a semiclassical analysis of the photoionization cross section for two-electron atoms, it is essential to have a good understanding of the underlying classical dynamics. The classical dynamics of two electrons in the field of a nucleus constitutes a three-body systems, which is nonintegrable with effectively four degrees of freedom. The overall dynamics are largely chaotic, most parts of the full phase space are still unexplored, however. An overview over the dynamics in some

important lower-dimensional invariant subspaces is given in Refs. [1,58]; more recent results on the dynamics near the triple collision can be found in Refs. [29,30], new insights into the global structure of the phase space were presented in Refs. [31,32,59].

The classical Hamiltonian for two-electron atoms with an infinitely heavy nucleus of charge $Z$ reads

$$H = \frac{\mathbf{p}_1^2 + \mathbf{p}_2^2}{2} - \frac{Z}{r_1} - \frac{Z}{r_2} + \frac{1}{r_{12}} = E, \tag{49}$$

with $r_{12}$ the electron-electron distance and $E$ the total energy. The double-ionization threshold corresponds to $E = 0$, here and we consider $E < 0$ in what follows. Making use of the scaling properties of the classical dynamics, we introduce the transformation

$$\begin{aligned} &\mathbf{r}_i = \tilde{\mathbf{r}}_i/|E|, \quad \mathbf{p}_i = \sqrt{|E|}\tilde{\mathbf{p}}_i, \quad S = \tilde{S}/\sqrt{|E|}, \\ &\mathbf{L} = \tilde{\mathbf{L}}/\sqrt{|E|}, \end{aligned} \tag{50}$$

where $\tilde{\mathbf{r}}_i$ and $\tilde{\mathbf{p}}_i$ correspond to coordinates and momenta at fixed energy $E = -1$, $S = \int \mathbf{p}d\mathbf{q}$ is the classical action integrated along a trajectory and $\mathbf{L}$ is the total angular momentum. Expressing $\mathbf{L}$ in scaled coordinates, we have $\tilde{\mathbf{L}} \to \mathbf{0}$ as $E \to 0$ when $\mathbf{L}$ remains constant. We can thus restrict the analysis to the three degrees of freedom subspace $\tilde{L} = 0$ if we work at fixed $\mathbf{L}$ and in the limit $E \to 0$ [30,60].

Following standard semiclassical arguments, the Green function $G(R,\mathbf{\Omega},R',\mathbf{\Omega}';E)$ can be approximated by contributions from classical trajectories at energy $E$ with initial and final coordinates given by $(R',\mathbf{\Omega}')$ and $(R,\mathbf{\Omega})$, respectively [61]. Likewise, the quantum scattering maps $\mathbf{s}, \mathbf{r}$ featuring in Eq. (20) can asymptotically be written as sums over trajectories starting and ending on the dividing surface $\Sigma$, that is, at $R = R' = R_0$ [43,44]. The dominant semiclassical contributions to the photoionization cross section are thus due to trajectories starting and ending in the phase-space region $R \leqslant R_0$.

In scaled coordinates, this region shrinks to zero according to $\tilde{R}_0 = |E|R_0 \to 0$ as one approaches the double-ionization threshold at $E = 0$. The part of the dynamics contributing to the cross section is thus formed by trajectories starting and ending closer and closer to the origin. For *regular* potentials, Eqs. (2) or (22) can be written in terms of closed orbits immediately and contributions due to the finite radius become negligible in the semiclassical limit; this leads to standard COT. The situation is different here, as the nonregularizable triple collision singularity is at the origin $R = 0$ and stability properties of orbits starting and ending closer and closer to the origin in the limit $|E| \propto \tilde{R}_0 \to 0$ diverge. Asymptotically, these trajectories converge to a set of triple collision orbits starting and ending exactly in the singularity—we will refer to these orbits as *closed triple collision orbits* (CTCO's). Triple collision orbits can only occur in the so-called $eZe$ space [30], a collinear subspace of the full three-body dynamics where the two electrons are on opposite sides of the nucleus [58]. As $\tilde{R}_0 \to 0$, only orbits coming close to the $eZe$ space can start and return to $\tilde{\Sigma}$ and they will do so in the vicinity of a CTCO. This implies that the photoionization signal is asymptotically determined by the dynamics in the $eZe$ space alone—a fact that was recently confirmed by experimental results and numerical calculations presented in Refs. [22,24].

The dynamics in the $eZe$ space are relatively simple; it is conjectured to be fully chaotic with a complete binary symbolic dynamics generated by the stable and unstable manifolds of the triple-collision singularity [31,32,58]. In particular, for every finite binary symbols string there is a CTCO, the shortest being the so-called Wannier orbit (WO) of symmetric collinear electron dynamics. Some examples of short CTCO's together with an explanation of the symbol code are shown in Fig. 2. Note, that there exist infinitely many CTCO's and their number increases exponentially with both symbol length and period; see Table I for a list of CTCO's up to binary symbol length 5.

#### 2. *Stability properties of CTCO's*

For a semiclassical analysis, the dynamics in the vicinity of contributing trajectories are of importance. They are taken into account by calculating the linearized flow along a given trajectory; all the necessary information can then be extracted from the stability matrix of the classical orbit. For triple collision orbits (TCO), entries in the stability matrix diverge as the trajectories move directly into or out of the singularity; the orbits are *infinitely unstable* [62]. The rate of divergence has a direct influence on the quantum photoionization cross section as will be argued in Sec. IV C.

The stability matrix $\mathbf{M}$ of a trajectory in the $eZe$ space is best calculated in a local coordinate system on the manifold of constant energy and angular momentum and perpendicular to the trajectory. When considering the $eZe$ space embedded in the full 3D space, the relevant part of $\mathbf{M}$ in local coordinates has the form [58]

$$\mathbf{M} = \begin{pmatrix} \mathbf{m}^{\perp} & 0 & 0 \\ 0 & \mathbf{m}^{\perp} & 0 \\ 0 & 0 & \mathbf{m}^{\parallel} \end{pmatrix}. \tag{51}$$

Here, $\mathbf{m}^{\perp}$ and $\mathbf{m}^{\parallel}$ are $2 \times 2$ matrices describing the linearized dynamics perpendicular to and in the $eZe$ space, respectively. The former is degenerate due to the two linearly independent and equivalent directions, in which perturbations can be considered perpendicular to the $eZe$ configuration, see Appendix E.

TCO's escape from or approach the triple collision at $R = 0$ symmetrically along the $r_1 = r_2$ axis in the $eZe$ space, that is, along the WO [31,63], see also Fig. 2. The rate of divergence of stability matrix elements is thus to leading order the same for all CTCO's and coincides with that of the WO. The stability matrix elements of the latter can be calculated explicitly; the derivation is given in Appendix E. One obtains, in particular, for the matrix elements $\tilde{m}_{12}^{\parallel}, \tilde{m}_{12}^{\perp}$ of a specific CTCO $\gamma$ starting and ending at $\tilde{R}_0$ (for fixed $E = -1$),

$$\tilde{m}_{12}^{\parallel} \sim A_{\gamma}^{\parallel}\, \tilde{R}_0^{3/2-2\mu_{eZe}}; \quad \tilde{m}_{12}^{\perp} \sim A_{\gamma}^{\perp}\, \tilde{R}_0^{3/2-2\mu_{\mathrm{WR}}}, \tag{52}$$

to leading order as $\tilde{R}_0 \to 0$. Here, $A_{\gamma}^{\perp,\parallel}$ correspond to CTCO specific weights which are asymptotically independent of $\tilde{R}_0$. Furthermore

$$\mu_{eZe} = \frac{1}{4}\sqrt{\frac{100Z-9}{4Z-1}}, \quad \mu_{\mathrm{WR}} = \frac{1}{4}\sqrt{\frac{4Z-9}{4Z-1}}; \tag{53}$$

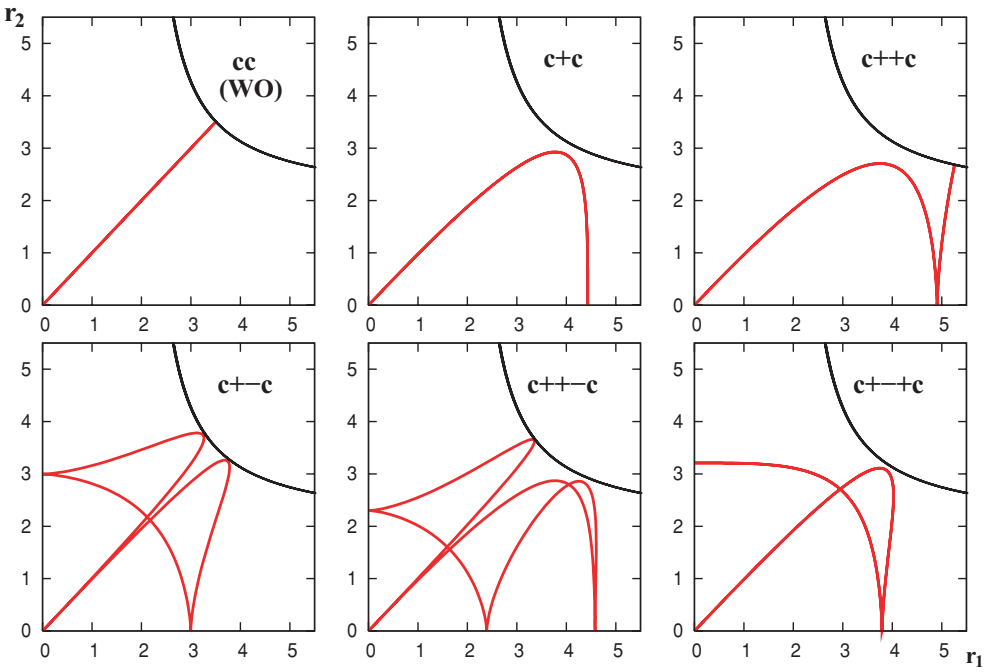


FIG. 2. (Color online) Some short CTCO's together with their symbol code at energy $E = -1$; the coordinates $r_1, r_2$ correspond to the distance of electron 1 or 2 from the origin in the collinear $eZe$ space. The code represents $c$: triple collision; $+$: binary collisions of electron 1 ($r_2 = 0$); $-$: binary collisions of electron 2 ($r_1 = 0$).

see Appendix E for details. Note that $\tilde{m}_{12}^{\perp}$ contributes only for $Z > 9/4$, that is, for real $\mu_{\mathrm{WR}}$. (The subscript WR refers to the Wannier ridge space; see the discussion in Appendix E.)

When approximating the Green function semiclassically, we are interested in matrix elements $m_{12}^{\parallel}$, $m_{12}^{\perp}$ for *constant* $R_0$ and in the limit $E \to 0$. The matrix elements $m_{12}$ relate initial

TABLE I. The classical action $S_\gamma$ and the stability matrix element $m_{12,\gamma}$ of CTCO along the $eZe$ degree of freedom, up to symbol length 5. The $a_\gamma^{\parallel}$ and $b_\gamma$ are fit parameters for Eq. (57), and $n_\gamma$ and $a_w$ denote the multiplicity of the orbit and the weight for the WO ($\gamma = \mathrm{cc}$), respectively.

| Symbol | $S_\gamma$(action) | $a_\gamma^{\parallel}$ | $b_\gamma$ | $n_\gamma a_\gamma^{\parallel}$ | $n_\gamma a_\gamma^{\parallel}/a_w^{\parallel}$ | $n_\gamma$ |
|---|---|---|---|---|---|---|
| $cc$ | 3.500 00 | 0.067 238 6 | 1.111 788 9 | 0.067 239 | 1.000 000 | 1 |
| $c+c$ | 5.246 81 | 0.050 670 0 | 1.111 788 9 | 0.101 340 | 1.507 169 | 2 |
| $c++c$ | 6.898 33 | 0.041 215 0 | 1.111 788 9 | 0.082 430 | 1.225 934 | 2 |
| $c+-c$ | 7.129 12 | 0.030 024 8 | 1.111 788 9 | 0.060 050 | 0.893 084 | 2 |
| $c+++c$ | 8.502 83 | 0.035 028 8 | 1.111 788 9 | 0.070 058 | 1.041 926 | 2 |
| $c++-c$ | 8.845 32 | 0.017 729 6 | 1.111 788 9 | 0.070 919 | 1.054 731 | 4 |
| $c+-+c$ | 8.934 25 | 0.025 876 7 | 1.111 788 9 | 0.051 753 | 0.769 698 | 2 |
| $c++++c$ | 10.078 37 | 0.030 625 0 | 1.111 788 9 | 0.061 250 | 0.910 936 | 2 |
| $c+++-c$ | 10.486 33 | 0.012 191 7 | 1.111 788 9 | 0.048 767 | 0.725 279 | 4 |
| $c++-+c$ | 10.626 65 | 0.018 617 1 | 1.111 788 9 | 0.074 468 | 1.107 524 | 4 |
| $c++--c$ | 10.573 94 | 0.009 569 3 | 1.111 788 9 | 0.019 139 | 0.284 637 | 2 |
| $c+-+-c$ | 10.777 52 | 0.016 517 4 | 1.111 788 9 | 0.033 035 | 0.491 308 | 2 |
| $c+--+c$ | 10.745 76 | 0.011 770 0 | 1.111 788 9 | 0.023 540 | 0.350 098 | 2 |
| $c+++++c$ | 11.630 46 | 0.027 309 3 | 1.111 788 9 | 0.054 619 | 0.812 312 | 2 |
| $c++++-c$ | 12.085 49 | 0.009 277 1 | 1.111 788 9 | 0.037 109 | 0.551 894 | 4 |
| $c++-+c$ | 12.258 63 | 0.013 556 0 | 1.111 788 9 | 0.054 224 | 0.806 444 | 4 |
| $c+++--c$ | 12.219 02 | 0.006 573 9 | 1.111 788 9 | 0.026 296 | 0.391 082 | 4 |
| $c++-++c$ | 12.301 06 | 0.015 653 7 | 1.111 788 9 | 0.031 307 | 0.465 617 | 2 |
| $c++-+-c$ | 12.485 13 | 0.009 881 6 | 1.111 788 9 | 0.039 526 | 0.587 851 | 4 |
| $c++--+c$ | 12.466 88 | 0.006 820 1 | 1.111 788 9 | 0.027 281 | 0.405 728 | 4 |
| $c+-++-c$ | 12.542 71 | 0.010 161 1 | 1.111 788 9 | 0.040 644 | 0.604 481 | 4 |
| $c+-+-+c$ | 12.598 71 | 0.013 450 4 | 1.111 788 9 | 0.026 901 | 0.400 079 | 2 |
| $c+---+c$ | 12.441 09 | 0.005 749 9 | 1.111 788 9 | 0.011 500 | 0.171 031 | 2 |

changes in momentum $\mathbf{p}'_\Omega$ to final changes in position $\mathbf{\Omega}$. One therefore obtains in scaled coordinates for trajectories starting and ending on the surface of section $\Sigma$

$$m_{12}(R_0) = |E|^{-3/2}\tilde{m}_{12}(\tilde{R}_0) = |E|^{-3/2}\tilde{m}_{12}(|E|R_0),$$

both for the $\perp$ and $\parallel$ degrees of freedom. Together with Eq. (52) and fixed initial condition $R_0$

$$m_{12}^{\parallel} \sim A_\gamma^{\parallel}\,|E|^{-2\mu_{eZe}}; \quad m_{12}^{\perp} \sim A_\gamma^{\perp}\,|E|^{-2\mu_{\rm WR}}, \tag{54}$$

as $|E| \to 0$ with $A_\gamma^{\parallel}$ and $A_\gamma^{\perp}$ now in leading order independent of energy. This universal scaling behavior of the stability matrix elements of CTCO's with respect to energy will form an integral part of the quantum scaling laws discussed in Sec. IV D.

#### 3. *The stability matrix of CTCO's and the exponent μ: numerical results*

For comparing semiclassical results with numerically exact quantum calculations, we determined the trajectories of all CTCO's up to symbol length 6 in collinear He. The symbol code is defined in the caption of Fig. 2, the CTCO data relevant for a semiclassical description are listed in Table I, (here for orbits up to symbol length 5). In particular, $S_\gamma$ is the classical action, $n_\gamma$ denotes the multiplicity, and $A_\gamma^{\parallel}$ is the prefactor defined in Eqs. (52) and (54) of a CTCO $\gamma$. The multiplicity is given by the number of different (but equivalent) orbits, which can be obtained through the symmetry transformations $r_1 \leftrightarrow r_2$ and time-reversal symmetry; ($n_\gamma$ can take on the values $n_\gamma = 1$, 2, or 4). Calculating the action $S_\gamma$ is straightforward. More care needs to be taken when calculating the prefactors $A_\gamma^{\parallel}$, $A_\gamma^{\perp}$. For this, we need to calculate the elements of the stability matrix (51) and to extrapolate $A_\gamma$ from the limit $\tilde{R}_0 \to 0$. Standard methods as described in Ref. [64] become unstable due to singularities in the equations of motion for the stability matrix elements.

We therefore calculate the stability matrix in Kustaanheimo-Stiefel (KS) coordinates, thereby regularizing the binary collision singularities [58]. There is a slight complication as time in KS coordinates depends explicitly on the coordinates $r_1$ and $r_2$; deviations in the time direction differ for the stability matrix $\mathbf{M}_{\rm KS}$ in KS space and $\mathbf{M}$ in real space along the CTCO. The part of the stability matrix perpendicular to the trajectory and on the energy manifold, that is, $\mathbf{m}^{\perp,\parallel}$ is, however, unaffected (up to a local linear coordinate transformation).

We can thus obtain the stability matrix elements using the relation

$$\mathbf{m}^{\parallel}(t) = (\mathbf{BA})^{-1}(t)\,\mathbf{m}_{\rm KS}^{\parallel}(t)\,(\mathbf{BA})(0), \tag{55}$$

and we will restrict our attention to $\tilde{m}_{ij}^{\parallel}$ for $eZe$ He in the following. Here, $\mathbf{B}(t)$ is the linearized transformation matrix from $eZe$ coordinates $z = (r_1, r_2, p_{r_1}, p_{r_2})$ to KS coordinates $Z$, that is,

$$B_{ij}(t) = dZ_i(t)/dz_j(t), \tag{56}$$

and $\mathbf{A}(t)$ is the projection matrix onto the coordinate space perpendicular to the trajectory defined in Ref. [64]. Since the $m_{12}$ elements of the stability matrices diverge for CTCO's as $R \to 0$, we calculated $m_{12}$ for a finite $R = R_0$. The stability matrix of a CTCO is determined numerically as a function of the hyperradius $R_0$ in the range $[10^{-7}, 10^{-2}]$, see Fig. 3. To improve the numerical accuracy, all calculations were done with $4 \times 8$-byte floating numbers instead of the usual 8-byte double precision. Numerically accuracy was checked against the condition $\det(\mathbf{m}^{\parallel}) = 1.0$, which is a basic property of the symplectic matrix. Using

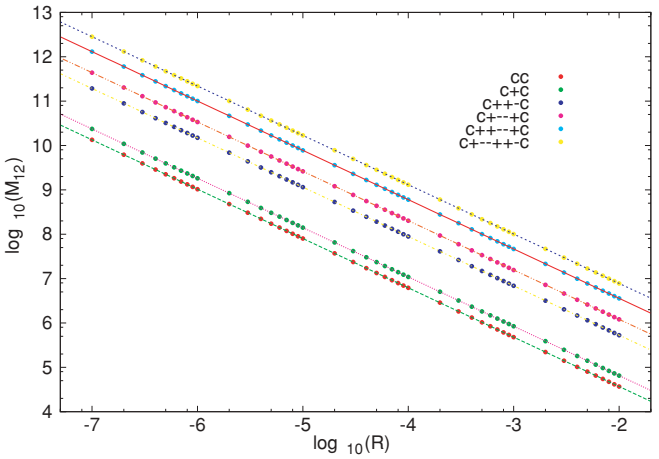


FIG. 3. (Color online) The stability matrix element $m_{12}^{\parallel}$ for some CTCO's on a log-log scale together with least-squares fits.

$$m_{12,\gamma}(R_0) = A_\gamma^{\parallel} R_0^{-b_\gamma}, \tag{57}$$

with $A_\gamma^{\parallel}, b_\gamma$ as fit parameters, one obtains $b_\gamma = 1.111\,789\,1$. Note that $b_{\rm theo} = -(3/2 - 2\mu_{eZe})$ with $\mu_{eZe}$ given in Eq. (53) and we obtain for He ($Z = 2$) $b_{\rm theo} = 1.111\,786\,4$ in very good agreement with the numerical results. We can thus extract numerical values for the weights $A_\gamma^{\parallel}$ along the $eZe$ degree of freedom. The results are listed in Table I where we set $a^{\parallel} = (A^{\parallel})^{-1/2}$; here, $a_w$ denotes the weight for the WO ($\gamma = cc$).

### C. Semiclassical approximation of the quantum scattering map r

The starting point for a semiclassical analysis of the photoionization cross section is Eq. (22). Our main goal is to obtain general information about the energy dependence of the cross section near the double-ionization threshold. In a first approximation, we will thus neglect contributions from closed channels; these can be taken into account by considering not only real, but also complex solutions of the classical equations of motion. The corresponding contributions are, however, exponentially suppressed in the semiclassical limit $E \to 0$. We may thus start from the formula for open channels, Eq. (B5), and write

$$\begin{aligned}\sigma(E) &= \sigma_0(E) + \sigma_{\rm fl}(E)\\ &= \frac{4\pi^2}{c}\omega{\rm Re}\left[\mathbf{d}^\dagger\left(1 + 2\sum_{n=1}^{\infty}(\mathbf{rs})^n\right)\mathbf{d}\right].\end{aligned} \tag{58}$$

(For the remainder of Sec. IV, only open channels are considered and we omit the subscripts for $\mathbf{s}_{oo}$, $\mathbf{r}_{oo}$, and $\mathbf{d}_o$). We identify the term $\mathbf{d}^\dagger\mathbf{d}$ with a background contribution $\sigma_0(E)$ varying smoothly as a function of energy across the threshold $E = 0$. The information about resonances is contained in the

sum over $n$, which is identified with $\sigma_{\rm fl}(E)$ here. It gives rise to a wildly fluctuating signal in the regime of strongly overlapping resonances when approaching the threshold; see Fig. 8. The terms $(\mathbf{rs})^n$ contain semiclassical contributions of orbits returning $n$ times to the surface of section $\Sigma$.

The dividing surface $\Sigma$ and thus $R_0$ are essentially determined by the initial state $\phi_0$ and are thus energy independent. From the definition of the inner scattering matrix $\mathbf{s}$ and the scattering solutions $\mathbf{\Psi}^{\pm}$ given in Eqs. (9) and (10), it is obvious that these operators are also not affected by the threshold. The half-scattering Hamiltonian $H_0$ defined in Eq. (8) contains no information about the threshold, which is specified by the behavior of the full potential in the limit $R \to \infty$. *Both* $\mathbf{s}$, $\mathbf{\Psi}^{\pm}$ *and thus* $\mathbf{d}$ *can therefore be regarded as constant for energies sufficiently close to the threshold*. The main information about the increasing number of overlapping resonances near the threshold is contained in the reflection matrix $\mathbf{r}$ alone.

A semiclassical approach is expected to give good results in regions sufficiently far from the origin; the semiclassical approximation will fail close—on the scale of a typical wave length—to the triple collision singularity due to the diverging slope of the potential in this region. (Note, that binary collisions do not pose difficulties here, as they can be regularized both from a quantum and classical point of view). After making $R_0$ sufficiently large, semiclassical approximations can be employed for the reflection operator $\mathbf{r}$, whereas the same does not necessarily hold for the operators $\mathbf{s}$ and $\mathbf{\Psi}^{\pm}$. Their contributions need to be treated fully quantum mechanically and thus numerically. They give rise to slowly varying terms across the threshold $E = 0$, see Sec. V.

The operator $\mathbf{r}$ can be written in semiclassical approximation [39,40,43,44] as

$$\mathbf{r}(\mathbf{\Omega},\mathbf{\Omega}',E) \approx (2\pi i)^{-\frac{f-1}{2}} \sum_j |\det \mathbf{M}_{12}|_j^{-1/2} e^{iS_j - i\pi\nu_j/2}, \quad (59)$$

where the sum is taken over all classical paths $j$ with fixed energy $E$ starting at points $\mathbf{\Omega}'$ on the surface of section $\Sigma$ (with momentum pointing outward) and ending at $\mathbf{\Omega}$ again on $\Sigma$ without crossing the surface of section in between. $S_j(\mathbf{\Omega},\mathbf{\Omega}';E)$ is the action of that path, $\nu_j$ is the Maslov index and $f$ denotes the number of degrees of freedom (with $f = 4$ for two-electron atoms in three dimensions and fixed angular momentum). Furthermore,

$$\det \mathbf{M}_{12} = \det\left(\frac{\partial^2 S}{\partial\mathbf{\Omega}\partial\mathbf{\Omega}'}\right)^{-1} = \det\left(\frac{\partial\mathbf{\Omega}}{\partial\mathbf{p}'_{\Omega}}\right), \quad (60)$$

where $\mathbf{p}_{\Omega}$ are the momentum variables conjugated to $\mathbf{\Omega}$. The $(f-1)\times(f-1)$ matrix $\mathbf{M}_{12}$ forms a submatrix of the $2(f-1)$ dimensional stability matrix describing the linearized Poincaré map on $\Sigma$ for fixed energy and angular momentum.

### D. CTCO's and scaling laws

Returning to the cross section (58), we will focus on the fluctuating part $\sigma_{\rm fl}(E)$ containing information about the resonance spectrum. The smooth contribution $\sigma_0(E)$ was calculated numerically in Sec. V, see Fig. 6.

In the limit $E \to 0$, which is equivalent to the limit $\tilde{R}_0 \to 0$ for fixed energy, swarms of trajectories starting from and returning to $\Sigma$ will do so close to the $eZe$ subspace. Trajectories which emerge from the vicinity of the triple collision and enter into a region of chaotic two-electron dynamics before returning to the triple collision can do this only by staying in the neighborhood of a CTCO [30]. In the limit $\tilde{R}_0 \to 0$, all returning orbits on $\Sigma$ converge to one of the CTCO's with actions and stabilities approaching those of the CTCO trajectory. The actions and Maslov indices become independent of $\mathbf{\Omega}',\mathbf{\Omega}$ asymptotically.

The reflection operator $\mathbf{r}(\mathbf{\Omega},\mathbf{\Omega}',E)$ can thus be written as a sum over all CTCO's starting and ending at $\Sigma$. The amplitudes in Eq. (59) corresponding to trajectories staying in the vicinity of a CTCO $\gamma$ with initial and final positions $\mathbf{\Omega}',\mathbf{\Omega}$ on $\Sigma$ take on the form

$$|\det \mathbf{M}_{12}(\mathbf{\Omega},\mathbf{\Omega}';E)|_\gamma^{-1/2} = |(m_{12}^{\perp})^2 m_{12}^{\parallel}|^{-1/2} \approx a_\gamma(\mathbf{\Omega},\mathbf{\Omega}')|E|^{\mu}, \quad (61)$$

with

$$\mu = \mu_{eZe} + 2\mu_{\rm WR} = \frac{1}{4}\left[\sqrt{\frac{100Z-9}{4Z-1}} + 2\sqrt{\frac{4Z-9}{4Z-1}}\right], \quad (62)$$

and $\mu_{eZe}$, $\mu_{\rm WR}$ given in Eq. (53) and derived in Appendix E. Equation (61) follows from the block diagonal structure of the stability matrix, see Eq. (51), and from the energy scaling given in Eq. (54). Note, that the overall amplitude in $\mathbf{r}$ and thus the amplitude of the fluctuating contribution $\sigma_{\rm fl}$ vanishes at the threshold. $\sigma_0$, on the other hand, continues smoothly across the threshold becoming the resonance-free single-ionization signal above the double-ionization threshold.

Including the contribution from the initial wave function $\phi_0$, we can write

$$\mathbf{d}^\dagger \mathbf{r} \mathbf{s} \mathbf{d} = \mathbf{d}^\dagger \mathbf{r} \mathbf{d}^* \approx (2\pi i)^{-\frac{f-1}{2}} |E|^{\mu} \sum_{\mathrm{CTCO}_\gamma} a_\gamma e^{iz\tilde{S}_\gamma - i\pi\nu_\gamma/2},$$

with $z = 1/\sqrt{|E|}$ and $\tilde{S}_\gamma$ is the action of the CTCO $\gamma$ for $E = -1$. The amplitude is formally obtained by integrating over $\Sigma$, that is,

$$a_\gamma = \sum_{n,n'\in\text{open}} \int_\Sigma d\mathbf{\Omega} d\mathbf{\Omega}' d_n^* \psi_n^*(\mathbf{\Omega};R_0) a_\gamma(\mathbf{\Omega},\mathbf{\Omega}') \psi_{n'}(\mathbf{\Omega}';R_0) d_{n'}^*,$$

where $\psi_n$ denotes the channel functions introduced in Eq. (7). Note that $a_\gamma$ depends on the ratio of the linear instability of a specific CTCO $\gamma$ to that of the WO as well as on the initial state $\phi_0$ and the scattering processes in the region $R < R_0$; they are to leading order independent of the energy and can be treated as constants across the threshold. Due to the universal behavior of the dynamics near the triple collision, the orbit-dependent terms $a_\gamma$ are up to an overall factor well described by the semiclassical weight alone. That is,

$$a_\gamma \approx |E|^{-\mu} |(m_{12}^{\perp})^2 m_{12}^{\parallel}|_\gamma^{-1/2} \approx |(A_\gamma^{\perp})^2 A_\gamma^{\parallel}|^{-1/2}, \quad (63)$$

where the rescaled matrix elements of the stability matrix are calculated directly along a CTCO $\gamma$. The numerical amplitudes $A_\gamma$ are defined in Eq. (54), the numerical values for the semiclassical weights $a_\gamma$ are listed in Table I.

The energy scaling (61) leads to a strong suppression of contributions from $(\mathbf{rs})^n$, $n > 1$ in Eq. (58). Semiclassically, they contain contributions from trajectory passing $n$ times through the section $\Sigma$. One expects an energy scaling of

these terms of the form $(\mathbf{rs})^n \sim |E|^{n\mu}$. We may thus neglect contributions with $n > 1$ in the limit $E \to 0$ and write $\sigma_{\rm fl}$ in terms of the first return map $\mathbf{r}$ alone; that is,

$$\sigma_{\rm fl}(E) \approx \frac{8\pi^2\omega}{c}\mathrm{Re}\,\mathbf{d}^\dagger\mathbf{r}\mathbf{d}^* \approx \frac{8\pi^2\omega}{c}\,|E|^\mu\,\mathrm{Re} \times \left[(2\pi i)^{-\frac{f-1}{2}}\sum_{\mathrm{CTCO}_\gamma} a_\gamma e^{iz\tilde{S}_\gamma - i\pi\nu_\gamma/2}\right]. \quad (64)$$

The relation (64) is the main result of this section. It predicts that the overall amplitude of the fluctuations decays with an exponent $\mu$ given by Eq. (62) derived from the triple collision dynamics. Note that this exponent is different from Wannier's exponent $\mu_w$ with [9]

$$\mu_w = \frac{1}{4}\sqrt{\frac{100Z-9}{4Z-1}} - \frac{1}{4}, \quad (65)$$

which describes the energy scaling of the double-ionization yield *above* threshold. One obtains, for example for He, $\mu = 1.305\,89\ldots$ compared to $\mu_w = 1.055\,89\ldots$; the WR contributes to the decay for $Z > 9/4$ when $\mu_{\rm WR}$ is real.

Equation (64) relates the oscillatory part of the single-ionization cross section to a "Fourier-type" expansion in terms of CTCO's with frequencies given by the actions of these orbits. The next section is devoted to testing these semiclassical results using the numerical tools developed in Sec. III.

## V. NUMERICAL RESULTS

A numerical study of the full three-body quantum problem is still out of reach for energies $E > I_N$ with $N \sim 20$ [21–23]; we therefore chose a model system, namely the $eZe$ collinear He, which was first studied quantum mechanically in Ref. [65] and later treated semiclassically in Refs. [66,67].

### A. Adiabatic potentials and channel functions

For the collinear $eZe$, the adiabatic Hamiltonian (5) is reduced to

$$H_R = \frac{1}{R^2}\left[-\frac{1}{2}\frac{\partial^2}{\partial\alpha^2} - \frac{1}{8} + RV(\alpha)\right], \quad (66)$$

where

$$V(\alpha) = -\frac{Z}{\cos\alpha} - \frac{Z}{\sin\alpha} + \frac{1}{\cos\alpha + \sin\alpha}. \quad (67)$$

We compute the adiabatic potentials $U_n(R)$ and channel functions $\psi_n(\alpha;R)$ by using $B$-spline basis functions. Because of the singularities at $\alpha = 0$ and $\alpha = \pi/2$, we take $\psi_n(0;R) = \psi_n(\pi/2;R) = 0$ as boundary conditions. The adiabatic Hamiltonian $H_R$ is invariant under the exchange of the two electrons, that is, $\alpha \to (\pi/2 - \alpha)$. Thus the range of $\alpha$ can be effectively reduced to $[0,\pi/4]$ by imposing the boundary conditions $\psi_n(0;R) = \psi_n(\pi/4;R) = 0$ for channel functions with odd parity and $\psi_n(0;R) = \psi_n'(\pi/4;R) = 0$ for those with even parity. These boundary conditions can be easily treated in the B-spline method following the prescription given in Ref. [68]. B-splines are taken up to order $k = 9$ and the breakpoints for $\alpha$ are chosen such that they concentrate near $\alpha = 0$ according to the exponential sequence

$$\alpha_i = \frac{\pi}{4}\frac{e^{\zeta(i-1)/(N_b-1)} - 1}{e^\zeta - 1} \quad \text{for} \quad i = 1,\ldots,N_b. \quad (68)$$

The region where the lowest eigenfunctions $\psi_n(\alpha;R)$ have significant magnitudes shrinks around $\alpha = 0$ as $R$ increases and thus $\zeta$ is chosen to increase accordingly. For example, $\zeta \sim 2$ is used for small $R < 1000$, while we choose $\zeta \sim 8$ for $R = 30\,000$ such that the density of breakpoints is highly localized near $\alpha = 0$. The number of points $N_b$ is varied as energy increases. For the range $I_{10}$ to $I_{15}$, we take $N_b = 600$, but increase to $N_b = 1100$ for $I_{45}$ to $I_{50}$. By varying the parameters $\zeta$ and $N_b$, we can easily obtain the adiabatic potentials and channel wave functions at each $R$ with a nine-digit accuracy in convergence of the potentials. The computational results for adiabatic potentials with odd and even parities in the range $R = [0,40]$ are shown in Fig. 4.

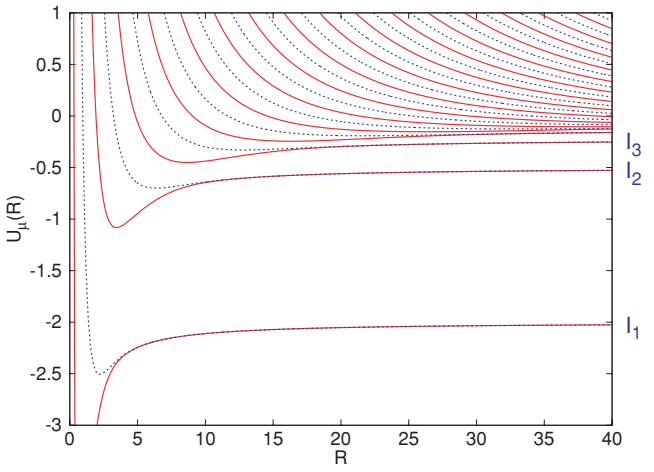


FIG. 4. (Color online) Adiabatic potentials for even (red line) and odd (blue dotted line) parities.

### B. The smooth part of the photoionization cross section $\sigma_0$

To obtain the smooth background part of total photoionization cross section $\sigma_0(E)$, according to Eq. (22), we need to calculate the initial wave function $\phi_0(R,\alpha)$ and the scattering wave function $\mathbf{\Psi}^+(R,\alpha)$ in Eq. (9).

#### 1. *The initial-state wave function*

The lowest odd-parity state is taken as the initial bound state $\phi_0$. For this eigenvalue problem, we use the matching method introduced in Ref. [69]. The boundary conditions for $\mathbf{F}(R)$ are written as $\mathbf{F}(0) = \mathbf{F}(R_0) = \mathbf{0}$ since $\phi_0(R,\alpha)$ is assumed nonzero only for $0 < R < R_0$. Choosing a matching radius $R_m < R_0$, $\mathbf{L}(0,R_m)$ is calculated by using the algorithm presented in Appendix C1, while the backward propagation method described in Appendix C2 is used for $\mathbf{L}(R_m,R_0)$. The matching condition is written as

$$[\mathbf{L}^{(4)}(0,R_m) - \mathbf{L}^{(1)}(R_m,R_0)]\mathbf{F}(R_m) = 0. \quad (69)$$

The bound-state energy is obtained by searching for an energy at which

$$\det[\mathbf{L}^{(4)}(0,R_m) - \mathbf{L}^{(1)}(R_m,R_0)] = 0. \quad (70)$$

For this purpose one can use the secant method or the bisection method as a searching algorithm. The solution of Eq. (70) is dependent on the parameters such as the radius $R_0$, the step size $h$ (see Appendix C 1), and the number of coupled channels $M$ defined in Sec. III. A converged energy of the lowest odd-parity state $E_0 = -2.225\,450\,395\,8$ is obtained with $h = 0.05$, $M = 30$, and $R_0 = 20.0$. With the bound-state energy $E_0$, $\mathbf{F}(R_m)$ is obtained by solving Eq. (69). Then the function $\mathbf{F}(R)$ over all ranges may be obtained from the relation

$$\mathbf{F}(R_k) = [\mathbf{L}^{(2)}(0,R_k)]^{-1}\mathbf{L}^{(2)}(0,R_m)\mathbf{F}(R_m),$$

for $R_k \in [0,R_m]$ and

$$\mathbf{F}(R_k) = [\mathbf{L}^{(3)}(R_k,R_0)]^{-1}\mathbf{L}^{(3)}(R_m,R_0)\mathbf{F}(R_m),$$

for $R_k \in [R_m,R_0]$. But one can easily find that this algorithm for $\mathbf{F}(R)$ is highly unstable since the quantities $\mathbf{F}'(0) = \mathbf{L}^{(2)}(0,R_m)\mathbf{F}(R_m)$ and $\mathbf{F}'(R_0) = \mathbf{L}^{(3)}(R_m,R_0)\mathbf{F}(R_m)$ have very small magnitudes for bound states. Thus, we adapt an alternative algorithm [70], which was originally developed for stable calculations of the radial function in the generalized log-derivative method [71]. In the SVD $L$-propagation method, the recursion relations for the radial function $\mathbf{F}(R)$ are written as

$$\mathbf{F}(R_{k-2}) = \mathbf{z}_{k-2}^{-1}\mathbf{O}(R_{k-2},R_{k-1})\mathbf{z}_{k-1}^{-1}\mathbf{O}(R_{k-1},R_k)\mathbf{F}(R_k), \quad (71)$$

for $R \in [0,R_m]$ with $\mathbf{z}_k = h\mathbf{L}^{(4)}(0,R_k) + [\mathbf{I} - h\mathbf{S}(R_k)]$ and

$$\mathbf{F}(R_k) = \mathbf{z}_k^{-1}\mathbf{O}^T(R_{k-1},R_k)\mathbf{z}_{k-1}^{-1}\mathbf{O}^T(R_{k-2},R_{k-1})\mathbf{F}(R_{k-2}), \quad (72)$$

for $R \in [R_m,R_0]$ with $\mathbf{z}_k = \mathbf{I} - h\mathbf{S}(R_k) - h\mathbf{L}^{(1)}(R_k,R_0)$ (see Appendix C 3 for more details). It is noted that these recursion relations enable one to obtain $\mathbf{F}$ only at the points $R_k$ with even $k$'s. To increase the accuracy in the numerical estimate of integrals containing wave functions such as the atomic dipole vector, we developed a method to obtain $\mathbf{F}$ additionally at midpoints of sectors, that is, at $R_k$'s with odd $k$'s (see Appendix C 4). In Fig. 5 the wave function of the lowest odd-parity state is plotted with $M = 10, h = 0.1$, and $R_0 = 20$.

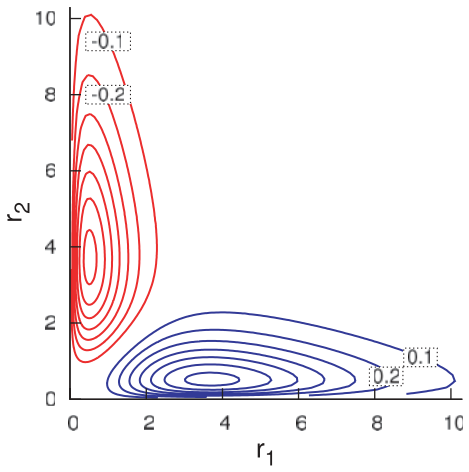


FIG. 5. (Color online) A contour plot of the wave function of the lowest odd-parity state.

### 2. *The scattering wave function for the inner-space Hamiltonian*

The $L$ propagator $\mathbf{L}(0,R_0)$ is obtained by using the method in Appendix C 1 and the local scattering matrix $\mathbf{s}$ is evaluated by using Eq. (38). Then, $\mathbf{F}(R_0)$ is determined according to Eq. (9) for each $\Psi_n^+$. To represent the set of $\{\Psi_n^+, n = 1,\ldots,M\}$, that is, $\mathbf{\Psi}^+$, the meaning of the notation $\mathbf{F}$ is extended from a vector to an $M \times M$ matrix of which the $n$th column corresponds to the radial function vector of $\Psi_n^+$. Starting from the initial values $\mathbf{F}(R_0)$, one can obtain $\mathbf{F}(R)$ for $R < R_0$ by using the recursion relation (C34). However, noting that the $L$ propagators are real valued, it is more convenient to deal with a real-valued radial function matrix $\mathbf{F}^K(R)$ rather than with the complex valued $\mathbf{F}(R)$ [72]. The boundary condition for $\mathbf{F}^K(R)$ is written as

$$\mathbf{F}^K(R) = \frac{1}{\sqrt{2\pi}}[\mathbf{f}^K(R) + \mathbf{g}^K(R)\mathbf{K}] \quad \text{for} \quad R \geqslant R_0, \quad (73)$$

where $\mathbf{f}^K$ and $\mathbf{g}^K$ are diagonal matrices with the following components

$$f_i^K = \begin{cases} \dfrac{\sin(k_i(R-R_0))}{\sqrt{k_i}} & \text{for open channels} \\ \dfrac{e^{+\kappa_i(R-R_0)}}{\sqrt{2\kappa_i}} & \text{for closed channels,} \end{cases} \quad (74)$$

and

$$g_i^K = \begin{cases} \dfrac{\cos(k_i(R-R_0))}{\sqrt{k_i}} & \text{for open channels} \\ \dfrac{e^{-\kappa_i(R-R_0)}}{\sqrt{2\kappa_i}} & \text{for closed channels.} \end{cases} \quad (75)$$

The $K$ matrix $\mathbf{K}$ is then obtained as

$$\mathbf{K} = -[\mathbf{L}^{(4)}(0,R_0)\mathbf{g}^K(R_0) - \mathbf{g}'^K(R_0)]^{-1} \times [\mathbf{L}^{(4)}(0,R_0)\mathbf{f}^K(R_0) - \mathbf{f}'^K(R_0)]. \quad (76)$$

Once the $K$ matrix is determined, then $\mathbf{F}^K(R)$ for $R < R_0$ can be obtained by backward propagation. Then for all ranges of $0 < R \leqslant R_0$, we can obtain $\mathbf{F}(R)$ by just multiplying a matrix $\mathbf{T}^K$ as $\mathbf{F}(R) = \mathbf{F}^K(R)\mathbf{T}^K$, where $\mathbf{T}^K$ can be obtained from the relation between Eqs. (9) and (73) such as

$$\mathbf{T}^K = \left[\frac{1}{2}\begin{pmatrix} \mathbf{K}_{oo} + i & \mathbf{K}_{oc} \\ 0 & \sqrt{2}e^{i\pi/4} \end{pmatrix}\right]^{-1}. \quad (77)$$

As can be seen in Eq. (78), by exploiting the fact that $\mathbf{T}^K$ is independent of $R$, we do not need to multiply $\mathbf{T}^K$ at every $R$ when performing a numerical integral containing $\mathbf{F}(R)$. This enhances the advantage of employing $\mathbf{F}^K(R)$.

### 3. *Dipole transition amplitudes*

In the collinear $eZe$ He atom the dipole interaction term is written as $D = \boldsymbol{\pi}(\mathbf{r}_1 + \mathbf{r}_2) = r_1 - r_2 = R(\cos\alpha - \sin\alpha)$. The dipole transition amplitude from the lowest odd-parity state $\phi_0$ to a scattering state $\Psi_i^+$ with even parity is written as

$$d_i = \langle \Psi_i^+ | D | \phi_0 \rangle = \sum_{j,n}^{M} \sum_{n'}^{M_0} T_{ji}^K \int_0^{R_0} dR F_{nj}^K(R)\mathcal{D}_{nn'}(R)F_{n'}^0(R)R, \quad (78)$$

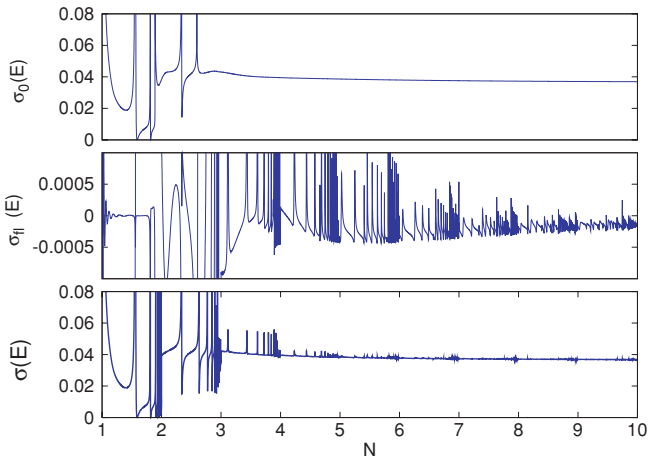


FIG. 6. (Color online) Total photoionization cross section $\sigma(E)$ of the lowest negative-parity state of the collinear He atom as a function of $N \equiv \sqrt{2/|E|}$ for the energy region of $[I_1, I_{10}]$. The parameters used are $h = 0.05$, $M = 20$, $N_b = 600$, $R_0 = 20$, and $R_\infty = 30,000$. In the uppermost figure, the smooth part $\sigma_0(E)$ is displayed, the middle figure shows the fluctuating part $\sigma_{\rm fl}(E)$, and the bottom panel is the total cross section $\sigma(E) = \sigma_0(E) + \sigma_{\rm fl}(E)$.

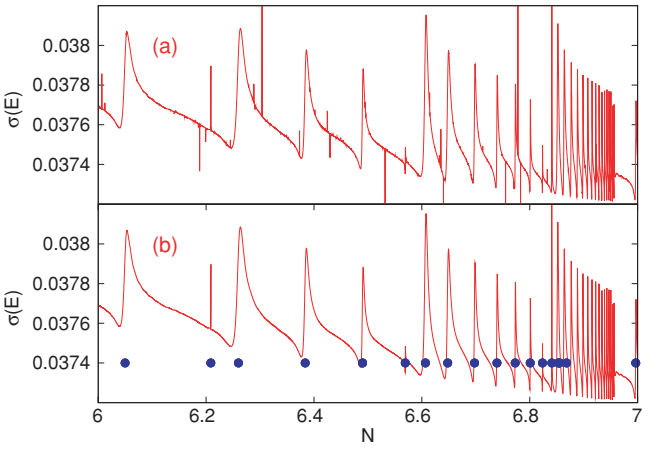


FIG. 7. (Color online) Comparison of (a) pure $L$ matrix and (b) $L$ and $S$ matrices propagation. Using pure $L$-matrix propagation one finds erroneous peaks, which disappear when switching to the mixed $L$- and $S$-matrices propagation. The parameters used are $M = 20$, $R_\infty = 2000$, $h = 0.05$, and $N_b = 600$. For comparison, the resonance poles obtained by using the complex rotation method are marked as solid circles in (b).

with

$$\mathcal{D}_{nn'}(R) = 2\int_0^{\pi/4} d\alpha \psi_n^e(\alpha;R)(\cos\alpha - \sin\alpha)\psi_{n'}^o(\alpha;R). \tag{79}$$

Here, $M$ and $M_0$ are the number of coupled channels for the scattering states and the initial-bound state, respectively, and $\boldsymbol{\psi}^e$ and $\boldsymbol{\psi}^o$ are the channel function vectors for even and odd parity. Furthermore, $\mathbf{F}^0$ is the radial function vector for the initial state, $\mathbf{F}^K$ and $\mathbf{T}^K$ are the real-valued radial function matrix and the transformation matrix to the complex-valued matrix for the scattering states $\boldsymbol{\Psi}^+$, respectively. The integral over the hyperangle $\alpha$ in Eq. (79) is performed by Gaussian quadrature rule, and the Simpson integral method is used for the radial integral in Eq. (78).

The smooth part of the photoionization cross section $\sigma_0 = (4\pi^2\omega/c)\mathbf{d}_o^\dagger \mathbf{d}_o$ is plotted as a function of $N \equiv \sqrt{2/|E|}$ in Fig. 6 for the energy region of $I_1$ to $I_{10}$. The parameter values used for the plot are $h = 0.05$, $M = 20$, $R_0 = 20$, and $N_b = 600$. There are some peaks in $\sigma_0$ for low energies $N < 3$. They are due to the resonant states localized in the region of $R < R_0$. However, as the energy increases, the support of resonant wave functions expands far beyond the boundary $R = R_0$ and thus their contribution to $\sigma_0$ becomes negligible. Actually, it can clearly be seen that $\sigma_0$ is smooth in the energy region beyond $N > 5$ and converges to a constant value as $N$ increases. If we choose a larger $R_0$, the resonant area extends to a larger energy. But there always exists a finite $N$ beyond which $\sigma_0$ is smooth.

### C. Fluctuating part of the photoionization cross section

#### 1. *Calculating the reflection matrix*

We already calculated **s** and **d**, so we only need to determine the reflection matrix **r** containing the information of the long-range Coulomb field. A direct calculation of the $L$ matrix $L(R_0, R_\infty)$ to the region $[R_0, R_\infty]$ is not possible computationally for large $R_\infty$ due to the lack of computer memory and computing time. But exploiting the $L$-matrix addition rule [34] enables us to calculate the $L$ matrix using parallel computing. We divide the full region $[R_0, R_\infty]$ into subintervals with nearly the same sizes. The number of the subintervals is equal to the number of CPU's of our parallel computer.

After propagating the $L$ matrices on each CPU to get $\mathbf{L}(R_0, R_\infty)$, we combine these contributions using the $L$-matrix addition rule. The matrix **r** can then be obtained using Eq. (36). The total photoionization cross section (TPICS) for $I_6$ to $I_7$ is plotted in Fig. 7 for the parameters $M = 20$, $R_\infty = 2000$, $h = 0.05$, and $N_b = 600$.

In a first attempt using the method described previously, we came across a number of peaks which were not stable under the change of parameters. An example of such a calculation is shown in Fig. 7(a). We therefore developed a new algorithm, called $S$-matrix propagation based on Ref. [73]. We first propagate the $L$ matrix for 20 steps and then we calculate the $S$ matrix for that interval using the boundary condition in Eqs. (74) and (75). Then using the $S$-matrix addition rule (see Appendix D), we can get the local scattering matrix **r**. In Fig. 7, we compare the TPICS obtained using pure $L$-matrix propagation and using a mixed $L$- and $S$-matrix propagation. The mixed propagation method manages to eliminate the unstable peaks in the in TPICS. We confirmed these results by comparing with the positions of the resonance poles obtained by using complex rotation method, which were calculated in connection with Ref. [33]. We used the mixing of $L$-matrix and $S$-matrix propagations in calculating the TPICS in other energy ranges as described previously.

In Fig. 8, the TPICS and its fluctuating part are plotted from $I_{10}$ to $I_{50}$. A smooth part of the TPICS is subtracted by fitting the signal in Fig. 8(a) with a linear function of the energy $E$

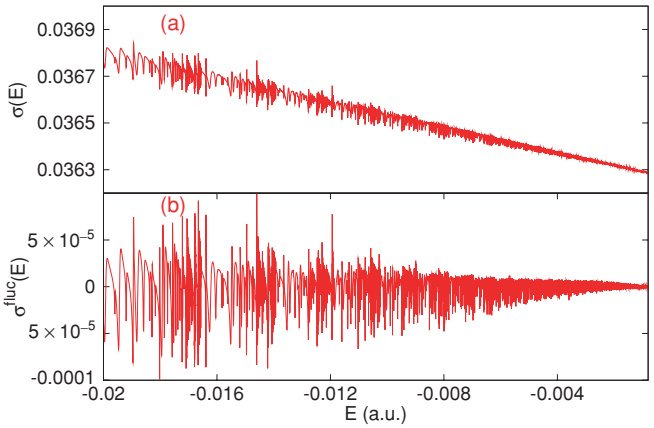


FIG. 8. (Color online) (a)Total photoionization cross section for range $N = [10, 50]$ and (b) its fluctuating part. The smooth part is subtracted by fitting a linear function in $E$ to the signal in (a).

and subtracting it to obtain $\sigma_{\rm fl}$ in Fig. 8(b). The parameters used in the calculation of the TPICS are shown in Table II.

### 2. *Action spectroscopy*

Having calculated the TPICS for collinear He up to the $N = 50$th ionization threshold, we return now to the semiclassical predictions, notably Eq. (64). It states that (i) the overall amplitude of the fluctuating part of the cross section as seen in Fig. 8(b) decays algebraically with an exponent given in Eq. (62) and (ii) that the signal can be decomposed in terms of contributions from CTCO's. The latter should give rise to distinct peaks at the position of the actions of CTCO's in the Fourier spectrum of $\sigma_{\rm fl}$. This can now be checked using our numerical quantum results. Note that for the collinear $eZe$ case $\mu_{\rm WR} = 0$.

We consider first point (ii), that is, the Fourier transform of the cross section. We define the following quantity

$$F(z) = \frac{1}{4\pi\alpha(E - E_g)|E|^{\mu}}\sigma_{\rm fl}(z), \tag{80}$$

where $z = 1/\sqrt{|E|}$ and $E_g$ is the energy of the initial state (such as shown in Fig. 5). The factor $|E|^{-\mu}$ compensates for the decrease in amplitude. Fourier transformation (FT) of $F(z)$ with respect to $z$ yields the spectrum shown in Fig. 9 where the solid line is the FT result of the quantum cross section. The position of the circles represents the classical action of a specific CTCO and the amplitudes as obtained from Eq. (63). More specifically, the height of the circles represents $n_\gamma a_\gamma$ of

TABLE II. The parameters used in the calculation of the TPICS.

| $N$ | $M$ | $R_\infty$ | h | $N_b$ |
|---|---|---|---|---|
| 10–15 | 30 | 30 000 | 0.05 | 600 |
| 15–20 | 40 | 30 000 | 0.05 | 600 |
| 20–25 | 50 | 30 000 | 0.05 | 700 |
| 25–30 | 60 | 50 000 | 0.05 | 800 |
| 30–35 | 70 | 60 000 | 0.05 | 900 |
| 35–40 | 80 | 80 000 | 0.05 | 1000 |
| 40–45 | 90 | 70 000 | 0.05 | 1000 |
| 45–50 | 100 | 80 000 | 0.05 | 1100 |

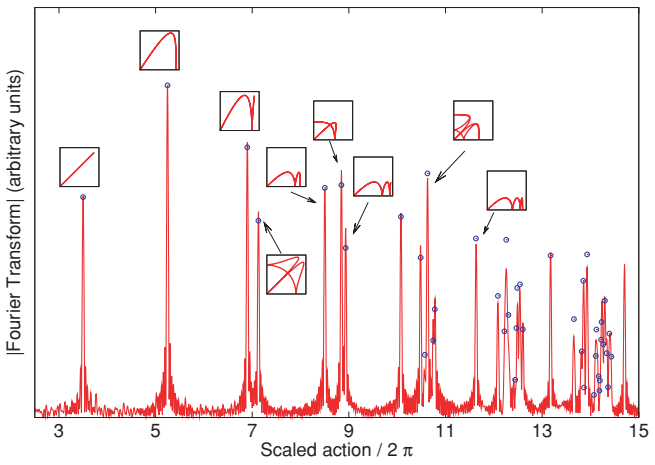


FIG. 9. (Color online) The Fourier spectrum of the fluctuating part of the $eZe$ cross section rescaled according to Eq. (80); the circles denote the position $\tilde{S}_j$ and (relative) size of $|M_{12}|_j^{-1/2}$ for CTCO's with $\tilde{S}/2\pi < 15$. The corresponding CTCO trajectories in configuration space are shown for some of the peaks in the insets.

a CTCO $\gamma$, where $a_\gamma$ is the semiclassical weight and $n_\gamma$ is the multiplicity of the CTCO, as given by the third through fifth columns of Table I. One clearly finds close agreement with the FT peak positions especially along the "action" axis, but also with the predicted amplitude.

### 3. *Estimating the exponent μ from the numerical data*

The semiclassical analysis in Sec. IV D predicts furthermore that the single photoionization cross section decays algebraically as $E \to 0^-$ with an exponent given in Eq. (62). Extracting a decay exponent from a strongly fluctuating signal such as shown in Fig. 8(b) is a somewhat delicate task. We use two different methods based on (a) fitting the signal $\sigma_{\rm fl}$ directly after suitable smoothing and (b) using the Fourier-transformed spectrum.

*a. Direct fitting method.* The cross-section data were determined numerically with a step size $\delta N = 0.001$ from $N = 10$ to $N = 50$ with $N = \sqrt{2}z = \sqrt{2/|E|}$. In the following, we average the absolute value of $\sigma_{\rm fl}(N)$ over fixed intervals of size $\Delta N$. When fitting an algebraic decay law to the smoothed data, it is advantageous to convolute the signal directly on a log-log scale, that is, we consider

$$\langle \log_{10}|\sigma_{\rm fl}(N)|\rangle_{\Delta N} = \frac{1}{\Delta}\int_{\log_{10}(N-\Delta N/2)}^{\log_{10}(N+\Delta N/2)} \log_{10}|\sigma_{\rm fl}(N)| d\log_{10} N,$$

where $\Delta = \log_{10}(N + \Delta N/2) - \log_{10}(N - \Delta N/2)$. In this way, we avoid artifacts due to the variation in curvature in the original curve $|\sigma_{\rm fl}(N)|$ when using large averaging intervals. The results are shown in Fig. 10; the smoothed data show a linear behavior (on the log-log scale) in line with expectations.

We now extract the slope of the curve in Fig. 10 using a linear regression model with least-squares fitting, that is, we assume

$$\langle \log_{10}|\sigma_{\rm fl}(\log_{10} N)|\rangle_{\Delta N} \approx a - 2b\log_{10} N,$$

with fit parameters $a$ and $b$.

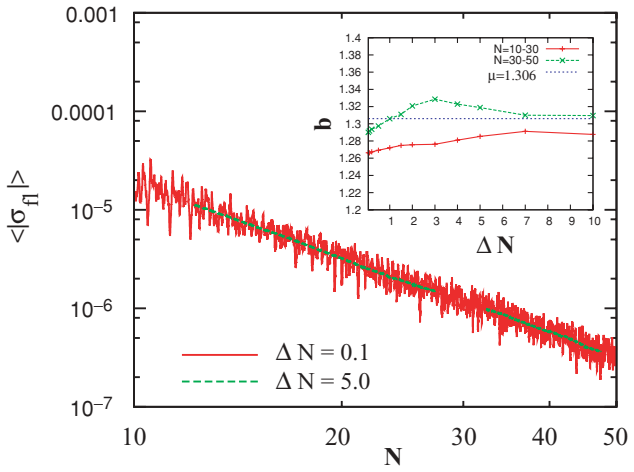


FIG. 10. (Color online) The modulus of $\sigma_{\rm fl}$ smoothed over an interval $\Delta N = 0.1$ (red line) and $\Delta N = 5.0$) (green line) on a log-log scale; inset: extracted $b$ values from two different set of data ($N = [10,30]$: red line: $N = [30,50]$: green line) and the expected value for collinear He, $\mu = 1.3059\ldots$.

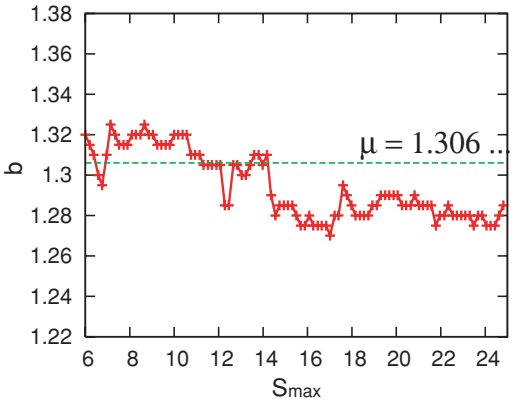


FIG. 11. (Color online) The exponents $b$ obtained from optimizing the FT data.

A detailed analysis revealed, however, another difficulty. The data were produced numerically by adjusting certain parameters as $N$ increases, see Table II. While care was taken to ensure a smooth transition at the points where parameters were altered, there are still minute discontinuities, in particular in $\sigma_0$, of the order of 0.0001%. When subtracting $\sigma_0$ numerically by fitting a linear curve to the data in Fig. 8(a), these discontinuities become noticeable after performing averages.

We identified two regions where these discontinuities were small, namely $N = 10 - 30$ and $N = 30 - 50$ and determined $\sigma_0$ separately for both data sets. We then determined the slope of the averaged $|\sigma_{\rm fl}|$ again for both regions separately; the results for the fit parameter $b$ for each of these intervals are shown in the inset of Fig. 10 for different averaging intervals $\Delta N$. The data coincide with the expected value within ±3%, that is, we obtain an exponent of the order $\mu = 1.3 \pm 0.04$.

*b. Fourier transform method.* To avoid the problem of discontinuities in the raw data, we devised a complementary technique based on the Fourier spectrum. The idea is to treat $\mu$ in Eq. (80) as a free parameter, $b$ say, and to find the value of $b$, which is consistent across the whole range of the cross-section data available. To this end, we divided the total range $N = 10 - 50$ into two parts, $N = 10 - 30$ and $N = 30 - 50$, respectively; we then obtain the action spectrum for a given value of $b$ for both sets of data separately, that is, we determine the Fourier transform

$$G(S;z_1,z_2) = \frac{1}{z_2 - z_1}\int_{z_1}^{z_2} F(z)e^{-iSz}dz, \qquad (81)$$

in the interval $z_1, z_2$ with $z = N/\sqrt{2}$. We now chose $b$ such that $G(S)$ becomes independent of the range of integration for the two intervals. This is, in practice, difficult to verify directly, so we actually determine the difference $|G(S;z_1,z_2)| - |G(S;z_2,z_3)|$ integrated over an $S$-interval with $S \in [S_{\rm min}, S_{\rm max}]$. The optimal $b$ is chosen such that this difference is minimized for a given value of $S_{\rm max}$. In Fig. 11, the optimal $b$ is plotted for a range of $S_{\rm max}$ values from 6 to 26 with a step size 0.2. The values obtained are of the order $\mu = 1.3 \pm 0.03$ in good agreement with the theoretical prediction Eq. (62), $\mu = 1.3059\ldots$. The error margins are similar to those obtained for fitting the cross-section data directly.

## VI. CONCLUSION

We present a theoretical framework together with numerical and semiclassical tools to gain access to the region of highly doubly excited states of the quantum spectra of two-electron atoms all the way to the double-ionization threshold. In particular, we introduce a quantum map approach which describes the total photoionization cross section in terms of quantum propagators acting on a dividing surface $\Sigma$ of constant hyperradius $R_0$. These quantum maps can be implemented effectively in a numerical scheme based on a variant of the log-derivative method. We give the details of the techniques for the special case of calculating the photoionization cross sections in the region of doubly excited states for two-electron atoms. The method was implemented numerically for collinear He making it possible to calculate the full cross section up to the 50th ionization threshold for the first time.

We furthermore present a semiclassical *closed triple collision orbit* theory including the derivation of the exponent $\mu$; these details were omitted in the original publication [33] where the threshold law was first presented. Using the numerically exact quantum data, the importance of the CTCO contributions can be confirmed quantitatively by considering the Fourier transformation of the fluctuating part of the cross section. A careful analysis of the quantum data also revealed an algebraic decay law for the amplitude of the cross section with an exponent consistent with the theoretical prediction with an error margin of ±3%.

The semiclassical analysis can be performed for one, two, or three spatial dimensions. While contributions by CTCO's were observed both in experimental data [20,74] and in 3D quantum calculations [75], a verification of the threshold law and the exponent $\mu$ is so far beyond the reach of existing 3D quantum results. Recent numerical calculations by Madroñero and co-workers on two-dimensional (2D) He [24] and 2D $Li^+$

[76] are pushing toward higher $N$ values and are getting into a regime where the full semiclassical theory can be tested. It will, in particular, be interesting to see how the dynamics along the Wannier ridge degree of freedom influences the details of the threshold law as predicted by Eq. (62).

## ACKNOWLEDGMENTS

This work was supported in part by the National Research Foundation of Korea Grant No. KRF-2007-314-C00120 and the Royal Society. We are very grateful to F. Mrugała for introducing the SVD generalized log-derivative method to us. We also wish to thank J. Eiglsperger and J. Madroñero for stimulating discussions regarding the exponent $\mu_{\rm WR}$ for 2D $Li^+$. The main calculations were performed using the supercomputing resource of the Korea Institute of Science and Technology Information (KISTI).

## APPENDIX A: THE GREEN FUNCTION $G_0$ ON $\Sigma$

In this Appendix, we derive the relation (15) for the coefficients of the half-scattering Green function $G_0(R,R')$ for $R > R_0; R' < R_0$ as given in Eq. (14). The retarded Green function $G_0$ fulfils Eq. (13) with respect to the Hamiltonian $H_0$ given in Eq. (8). It consists by definition only of outgoing waves in the region $R > R_0$ leading to the expansion (14).

Consider first the free Green function in a potential $V(\Omega)$, Eq. (6), and free motion along the $R$ axis with source point at $R'$, that is,

$$G_{\rm free} = -\sum_n \frac{i}{k_n} e^{ik_n|R-R'|}\psi_n(\mathbf{\Omega};R_0)\psi_n(\mathbf{\Omega}';R_0);$$

the sum is here again both over open and closed channels. Returning to the half-scattering problem Eq. (8), we can write for $R, R' > R_0$,

$$G_0(R,\mathbf{\Omega},R',\mathbf{\Omega}') = G_{\rm free} - i\sum_n \sqrt{\frac{2\pi}{k_n}} e^{ik_n(R'-R_0)}\psi_n(\mathbf{\Omega}';R_0)\Psi_n^+(R,\mathbf{\Omega}).$$

That is, the wave function can be decomposed into a direct contribution from the source point $R'$ (contained in $G_{\rm free}$) and a part reflected from the inner region around the origin (contained in the scattering solution $\Psi_n^+$). Likewise, we can consider the half-scattering Green function for $R < R_0$ (which has no direct component from $G_{\rm free}$), that is,

$$G_0(R,\mathbf{\Omega},R_0,\mathbf{\Omega}') = -i\sum_n \sqrt{\frac{2\pi}{k_n}} e^{ik_n(R'-R_0)}\psi_n(\mathbf{\Omega}';R_0)\Psi_n^+(R,\mathbf{\Omega}) \quad R' > R_0.$$

Using the symmetry of $G_0$, Eq. (12), which amounts to $G_0(R,\Omega,R',\Omega') = G_0(R',\Omega',R,\Omega)$ and comparing with Eq. (14) yields Eq. (15), that is

$$a_n = -2\pi i \Psi_n^+.$$

## APPENDIX B: THE CONNECTION BETWEEN $\Psi^+$ AND $\Psi^-$

Expressions for the total cross section such as those presented in Sec. II E were considered before by Granger and Greene [45] and also adopted in Refs. [33,48]. We will show here that our Eq. (22) contains the result in Ref. [45] in the limit when closed channels are neglected.

To simplify the notation, we write Eqs. (9) and (10) in the form

$$|\mathbf{\Psi}^+\rangle = |{\psi_{\rm in}}^-\rangle + \mathbf{s}^T|{\psi_{\rm out}}^+\rangle \tag{B1}$$

$$|\mathbf{\Psi}^-\rangle = |{\psi_{\rm in}}^+\rangle + \mathbf{s}^*|{\psi_{\rm out}}^-\rangle, \tag{B2}$$

with

$$\langle R,\mathbf{\Omega}|{\psi_{\rm in}}^+\rangle_n = \frac{1}{\sqrt{2\pi k_n^*}}\psi_n(\mathbf{\Omega};R_0)e^{ik_n^*(R-R_0)} \text{ for } R \geqslant R_0,$$

$$\langle R,\mathbf{\Omega}|{\psi_{\rm out}}^+\rangle_n = \frac{1}{\sqrt{2\pi k_n}}\psi_n(\mathbf{\Omega};R_0)e^{ik_n(R-R_0)} \text{ for } R \geqslant R_0,$$

and $|{\psi_{\rm in}}^-\rangle_n = |{\psi_{\rm in}}^+\rangle_n^*$, $|{\psi_{\rm out}}^-\rangle_n = |{\psi_{\rm out}}^+\rangle_n^*$. We write, as usual, channel eigenfunctions $\psi_n$ as real functions. Setting up the $\mathbf{s}$ matrix in the form

$$\mathbf{s} = \begin{pmatrix} \mathbf{s}_{oo} & \mathbf{s}_{oc} \\ \mathbf{s}_{co} & \mathbf{s}_{cc} \end{pmatrix},$$

where $\{o,c\}$ denotes open and closed components, and using general properties of scattering matrices following from flux conservation and the time-reversal symmetry [39,40], one obtains

$$\begin{gathered} \mathbf{s}_{oo}\mathbf{s}_{oo}^* = 1, \\ \mathbf{s}_{oo}\mathbf{s}_{oc}^* = -i\mathbf{s}_{oc} \quad \mathbf{s}_{co}\mathbf{s}_{oo}^* = i\mathbf{s}_{co}^*, \\ \mathbf{s}_{co}\mathbf{s}_{oc}^* = i(\mathbf{s}_{cc}^* - \mathbf{s}_{cc}), \end{gathered} \tag{B3}$$

together with

$$\mathbf{s} = \mathbf{s}^T. \tag{B4}$$

Using the definition of the scattering solutions where we write $|\mathbf{\Psi}^+\rangle = (|\mathbf{\Psi}_o^+\rangle, |\mathbf{\Psi}_c^+\rangle)^T$ and together with the relations, Eqs. (B3) and (B4), one obtains

$$|\mathbf{\Psi}^-\rangle = \begin{pmatrix} \mathbf{s}_{oo}^* & 0 \\ \mathbf{s}_{co}^* & i\mathbf{1} \end{pmatrix}|\mathbf{\Psi}^+\rangle.$$

Note, that we use the convention, such that $i|{\psi_{\rm in}}^-\rangle_c = |{\psi_{\rm in}}^+\rangle_c$ and $i|{\psi_{\rm out}}^+\rangle_c = |{\psi_{\rm out}}^-\rangle_c$.

These relations can be used to express Eqs. (19) and (20) in terms of $|\mathbf{\Psi}^+\rangle, \langle\mathbf{\Psi}^+|$ only. The result by Granger and Greene [45] follows, if one neglects contributions from closed channels and uses $\langle\mathbf{\Psi}_o^-| = \mathbf{s}_{oo}\langle\mathbf{\Psi}_o^+|$. That is, one writes the total cross section, Eq. (22), in the form

$$\begin{aligned} \sigma(E) &\approx \frac{4\pi^2}{c}\omega\,[\mathbf{d}_o^\dagger\mathbf{d}_o + 2\mathrm{Re}\,\mathbf{d}_o^\dagger(\mathbf{1}-\mathbf{r}_{oo}\mathbf{s}_{oo})^{-1}\mathbf{r}_{oo}\mathbf{d}_o^*] \\ &= \frac{4\pi^2}{c}\omega\,\mathrm{Re}\,\mathbf{d}_o^\dagger[\mathbf{1}+2(\mathbf{1}-\mathbf{r}_{oo}\mathbf{s}_{oo})^{-1}\mathbf{r}_{oo}\mathbf{s}_{oo}]\mathbf{d}_o \\ &= \frac{4\pi^2}{c}\omega\,\mathrm{Re}\,\mathbf{d}_o^\dagger\left[\frac{\mathbf{1}+\mathbf{r}_{oo}\mathbf{s}_{oo}}{\mathbf{1}-\mathbf{r}_{oo}\mathbf{s}_{oo}}\right]\mathbf{d}_o, \end{aligned} \tag{B5}$$

with $d_o = \langle\Psi_o^+|D|\phi_0\rangle = s_{oo}^T\langle\Psi_o^-|D|\phi_0\rangle$.

## APPENDIX C: SVD-TYPE ALGORITHM FOR THE EVALUATION OF THE *L* PROPAGATOR AND WAVE FUNCTIONS

### 1. *L* propagator by forward propagation

To evaluate the propagator $\mathbf{L}(R',R'')$, as mentioned in Sec. III C, we divide the interval $[R',R'']$ into $N$ sectors of length $2h$,

$$R_k = R_0 + kh,\ R_0 = R', \quad R_{2N} = R'' \quad \text{for} \quad k = 1, 2, \ldots, 2N. \tag{C1}$$

The matrices $\mathbf{L}(R_j,R_k)$ and $\mathbf{O}(R_k,R_{k+1})$ will be hereafter denoted by $\mathbf{L}_{j,k}$ and $\mathbf{O}_{k,k+1}$. For a given half-sector $[R_k,R_{k+1}]$, by using Eq. (48) and the explicit expression for $\mathbf{L}_{\bar{R}}(R_k,R_{k+1})$ in Ref. [34], it can be shown that [36]

$$\mathbf{L}_{k,k+1} = \begin{pmatrix} -\frac{1}{h}(\mathbf{I} - h\mathbf{S}_k) & \frac{1}{h}\mathbf{O}_{k,k+1} \\ -\mathbf{O}^T_{k,k+1}\frac{1}{h} & \frac{1}{h}(\mathbf{I} - h\mathbf{S}_{k+1}) \end{pmatrix}, \tag{C2}$$

where

$$h\mathbf{S}_k = \begin{cases} \frac{h^2}{3}\mathbf{w}_k & \text{for even } k \\ 4\mathbf{I} - \frac{1}{2}\left(\frac{1}{8} + \frac{1}{48}h^2\mathbf{w}_k\right)^{-1} & \text{for odd } k, \end{cases} \tag{C3}$$

with $\mathbf{w}_k = 2[E\mathbf{I} - \mathbf{U}(\mathbf{R_k})]$. Using Eq. (C2), the recursion relations resulting from the "addition" of $L$ propagators over subsequent intervals [34] can be written as

$$\mathbf{L}^{(1)}_{0,k+1} = \mathbf{L}^{(1)}_{0,k} - \mathbf{L}^{(2)}_{0,k}\mathbf{\Delta}_k^{-1}\mathbf{L}^{(3)}_{0,k}, \tag{C4}$$

$$\mathbf{L}^{(2)}_{0,k+1} = \mathbf{L}^{(2)}_{0,k}\mathbf{\Delta}_k^{-1}\mathbf{O}_{k,k+1}, \tag{C5}$$

$$\mathbf{L}^{(3)}_{0,k+1} = \mathbf{O}^T_{k,k+1}\mathbf{\Delta}_k^{-1}\mathbf{L}^{(3)}_{0,k}, \tag{C6}$$

$$\mathbf{L}^{(4)}_{0,k+1} = \frac{1}{h}(\mathbf{I} - h\mathbf{S}_{k+1}) - \frac{1}{h^2}\mathbf{O}^T_{k,k+1}\mathbf{\Delta}_k^{-1}\mathbf{O}_{k,k+1}, \tag{C7}$$

where

$$h\mathbf{\Delta}_k = h\mathbf{L}^{(4)}_{0,k} + (\mathbf{I} - h\mathbf{S}_k). \tag{C8}$$

Introducing the quantities

$$\mathbf{r}_k = \mathbf{L}^{(1)}_{0,k}, \quad \mathbf{p}_k = \mathbf{L}^{(3)}_{0,k} = -\left[\mathbf{L}^{(2)}_{0,k}\right]^T, \quad \mathbf{z}_k = h\mathbf{\Delta}_k, \tag{C9}$$

the forward recursion relations are written in terms of $\mathbf{r}$, $\mathbf{p}$, and $\mathbf{z}$ as

$$\mathbf{r}_k = \mathbf{r}_{k-1} + h\mathbf{p}^T_{k-1}\mathbf{z}^{-1}_{k-1}\mathbf{p}_{k-1}, \tag{C10}$$

$$\mathbf{p}_k = \mathbf{O}^T_{k-1,k}\mathbf{z}^{-1}_{k-1}\mathbf{p}_{k-1}, \tag{C11}$$

$$\mathbf{z}_k = -\mathbf{O}^T_{k-1,k}\mathbf{z}^{-1}_{k-1}\mathbf{O}_{k-1,k} + 2(\mathbf{I} - h\mathbf{S}_k), \tag{C12}$$

where the initial values for $\mathbf{r}_1$, $\mathbf{p}_1$, and $\mathbf{z}_0$ are given as

$$\mathbf{r}_1 = \frac{h}{3}\mathbf{w}_0 - \frac{1}{h}\mathbf{I}, \tag{C13}$$

$$\mathbf{p}_1 = -\frac{1}{h}\mathbf{O}^T_{0,1}, \tag{C14}$$

$$\mathbf{z}_0^{-1} = 0. \tag{C15}$$

In a final step, by converting the matrices $\mathbf{z}_{2N}$, $\mathbf{r}_{2N}$, and $\mathbf{p}_{2N}$ to the blocks of the propagator $\mathbf{L}_{0,2N}$, we obtain

$$\mathbf{L}^{(1)}_{0,2N} = \mathbf{r}_{2N}, \tag{C16}$$

$$\mathbf{L}^{(2)}_{0,2N} = -\mathbf{p}^T_{2N}, \tag{C17}$$

$$\mathbf{L}^{(3)}_{0,2N} = \mathbf{p}_{2N}, \tag{C18}$$

$$\mathbf{L}^{(4)}_{0,2N} = \frac{1}{h}\left(\mathbf{z}_{2N} + \frac{h^2}{3}\mathbf{w}_{2N} - \mathbf{I}\right). \tag{C19}$$

### 2. *L* propagator by backward propagation

Using the same procedure employed for the forward recursion relations (C4) through (C7), we can obtain the backward recursion relations in the form

$$\mathbf{L}^{(1)}_{k-1,2N} = -\frac{1}{h}(\mathbf{I} - h\mathbf{S}_{k-1}) + \mathbf{O}_{k-1,k}\mathbf{\Delta}_k^{-1}\mathbf{O}^T_{k-1,k},$$

$$\mathbf{L}^{(2)}_{k-1,2N} = \frac{1}{h}\mathbf{O}_{k-1,k}\mathbf{\Delta}_k^{-1}\mathbf{L}^{(2)}_{k,2N},$$

$$\mathbf{L}^{(3)}_{k-1,2N} = \frac{1}{h}\mathbf{L}^{(3)}_{k,2N}\mathbf{\Delta}_k{}^{-1}\mathbf{O}^T_{k-1,k},$$

$$\mathbf{L}^{(4)}_{k-1,2N} = \mathbf{L}^{(4)}_{k,2N} + \mathbf{L}^{(3)}_{k,2N}\mathbf{\Delta}_k{}^{-1}\mathbf{L}^{(2)}_{k,2N},$$

where

$$h\mathbf{\Delta}_k = \mathbf{I} - h\mathbf{S}_k - h\mathbf{L}^{(1)}_{k,2N}.$$

Introducing the working quantities

$$\mathbf{r}_k = \mathbf{L}^{(4)}_{k,2N}, \quad \mathbf{p}_k = \mathbf{L}^{(2)}_{k,2N}, \quad \mathbf{z}_k = h\mathbf{\Delta}_k, \quad \mathbf{t}_k = h\mathbf{L}^{(3)}_{k,2N}, \tag{C20}$$

the backward recursion relations are written as

$$\mathbf{r}_{k-1} = \mathbf{r}_k - h\mathbf{p}^T_k\mathbf{z}^{-1}_k\mathbf{p}_k, \tag{C21}$$

$$\mathbf{p}_{k-1} = \mathbf{O}_{k-1,k}\mathbf{z}^{-1}_k\mathbf{p}_k, \tag{C22}$$

$$\mathbf{z}_{k-1} = 2(\mathbf{I} - h\mathbf{S}_{k-1}) - \mathbf{O}_{k-1,k}\mathbf{z}^{-1}_k\mathbf{O}^T_{k-1,k}, \tag{C23}$$

$$\mathbf{t}_{k-1} = \mathbf{t}_k\mathbf{z}^{-1}_k\mathbf{O}^T_{k-1,k}, \tag{C24}$$

for $k = 2N-1, 2N-2, \ldots, 1$. By noting that

$$\mathbf{L}_{2N,2N} = \begin{pmatrix} -\mathbf{c} & \mathbf{c} \\ -\mathbf{c} & \mathbf{c} \end{pmatrix},$$

with the limit $\mathbf{c} \to \infty$ [34], we can show that the initial conditions are given by

$$\mathbf{r}_{2N-1} = \mathbf{L}^{(4)}_{2N-1,2N} = \frac{1}{h}(\mathbf{I} - h\mathbf{S}_{2N}), \tag{C25}$$

$$\mathbf{p}_{2N-1} = \mathbf{L}^{(2)}_{2N-1,2N} = \frac{1}{h}\mathbf{O}_{2N-1,2N}, \tag{C26}$$

$$\mathbf{z}_{2N-1} = h\mathbf{L}^{(4)}_{2N-2,2N-1} - h\mathbf{L}^{(1)}_{2N-1,2N} = 2(\mathbf{I} - h\mathbf{S}_{2N-1}), \tag{C27}$$

$$\mathbf{t}_{2N-1} = h\mathbf{L}^{(3)}_{2N-1,2N} = -\mathbf{O}^T_{2N-1,2N}. \tag{C28}$$

And, in a final step, we obtain the propagator $\mathbf{L}_{0,2N}$ from the matrices $\mathbf{r}_0$, $\mathbf{p}_0$, and $\mathbf{z}_0$ in the form

$$\mathbf{L}^{(1)}_{0,2N} = \frac{1}{h}\left[-\mathbf{z}_0 + \left(\mathbf{I} - \frac{h^2\mathbf{w}_0}{3}\right)\right], \tag{C29}$$

$$\mathbf{L}^{(2)}_{0,2N} = \mathbf{p}_0, \tag{C30}$$

$$\mathbf{L}^{(3)}_{0,2N} = -\mathbf{p}^T_0, \tag{C31}$$

$$\mathbf{L}^{(4)}_{0,2N} = \mathbf{r}_0. \tag{C32}$$

### 3. Recursion relations for $\mathbf{F}(R_k)$

First, let us consider the SVD $L$ propagation from $R=0$ to $R=R_m$ where $R_m$ is a matching point. From Eqs. (C9) and (C11), it can be shown that

$$\left[\mathbf{L}^{(2)}_{0,k-2}\right]^{-1}\mathbf{L}^{(2)}_{0,k}=\mathbf{z}^{-1}_{k-2}\mathbf{O}_{k-2,k-1}\mathbf{z}^{-1}_{k-1}\mathbf{O}_{k-1,k}, \tag{C33}$$

and thus

$$\mathbf{F}_{k-2}=\mathbf{z}^{-1}_{k-2}\mathbf{O}_{k-2,k-1}\mathbf{z}^{-1}_{k-1}\mathbf{O}_{k-1,k}\mathbf{F}_k, \tag{C34}$$

where we formally used the relation $[\mathbf{L}^{(2)}_{0,k-2}]^{-1}\mathbf{L}^{(2)}_{0,k}\mathbf{F}_k=\mathbf{F}_{k-2}$. Given $\mathbf{F}_m$, Eq. (C34) enables one to obtain $\mathbf{F}_k$ for $k=0$ to $k=m-2$ by using Eq. (C34).

Now let us consider the radial function for the remaining interval $R=[R_m,R_{2N}]$. Applying the backward recursion relation (C21) repeatedly and remembering that $\mathbf{t}_k=h\mathbf{L}^{(3)}_{k,2N}$, we obtain

$$\mathbf{L}^{(3)}_{k-2,2N}=\mathbf{L}^{(3)}_{k,2N}\mathbf{z}^{-1}_{k}\mathbf{O}^{T}_{k-1,k}\mathbf{z}^{-1}_{k-1}\mathbf{O}^{T}_{k-2,k-1}. \tag{C35}$$

Then, using the relation

$$\left(\mathbf{L}^{(3)}_{k,2N}\right)^{-1}\mathbf{L}^{(3)}_{k-2,2N}\mathbf{F}_{k-2}=\mathbf{F}_k,$$

we find the recursion relation

$$\mathbf{F}_k=\left(\mathbf{z}^{-1}_{k}\mathbf{O}^{T}_{k-1,k}\mathbf{z}^{-1}_{k-1}\mathbf{O}^{T}_{k-2,k-1}\right)\mathbf{F}_{k-2}. \tag{C36}$$

This makes it possible after starting from a given $\mathbf{F}_M$ to obtain $\mathbf{F}_k$ for $k=m+2$ to $k=2N$. It is remarkable that we only need to calculate $\mathbf{z}_k$ in both forward and backward propagations as can be seen in Eqs. (C34) and (C36). This effectively reduces the CPU time.

### 4. Radial functions at midpoints of sectors

As mentioned in Sec. V B1, it is desirable to evaluate radial functions at midpoints of sectors. Let us assume that, for a given sector $[\bar{R}-h,\bar{R}+h]$, there exist two $M\times M$ matrices $\mathbf{u}^{\pm}_{\bar{R}}(R)$ which are solutions of Eq. (42) with boundary conditions $\mathbf{u}^{+}_{\bar{R}}(\bar{R}-h)=\mathbf{u}^{-}_{\bar{R}}(\bar{R}+h)=\mathbf{I}$ and $\mathbf{u}^{+}_{\bar{R}}(\bar{R}+h)=\mathbf{u}^{-}_{\bar{R}}(\bar{R}-h)=\mathbf{0}$. Then, for $R\in[\bar{R}-h,\bar{R}+h]$, any solution $\mathbf{F}_{\bar{R}}(R)$ of Eq. (42) can be expressed as a linear combination of $\mathbf{u}^{\pm}_{\bar{R}}(R)$, that is,

$$\mathbf{F}_{\bar{R}}(R)=\mathbf{u}^{+}_{\bar{R}}(R)\mathbf{F}_{\bar{R}}(\bar{R}-h)+\mathbf{u}^{-}_{\bar{R}}(R)\mathbf{F}_{\bar{R}}(\bar{R}+h). \tag{C37}$$

Following Ref. [34], it can be shown that

$$\mathbf{u}^{\pm}_{\bar{R}}(\bar{R})=\frac{1}{2}\left[\mathbf{I}-\frac{1}{2}h^2\mathbf{w}_{\bar{R}}(\bar{R})\right]^{-1}, \tag{C38}$$

with the same accuracy as for the $L$ propagator. Thus, using $\mathbf{F}_{\bar{R}}(R)=\mathbf{O}^{T}(R,\bar{R})\mathbf{F}(R)$ and $\mathbf{w}_{\bar{R}}(\bar{R})=2[E\mathbf{I}-\mathbf{U}(\bar{R})]$, one can easily obtain $\mathbf{F}(\bar{R})$ from $\mathbf{F}(\bar{R}-h)$ and $\mathbf{F}(\bar{R}+h)$ with the help of

$$\begin{aligned}\mathbf{F}(\bar{R})=&\tfrac{1}{2}\{\mathbf{I}-h^2[E\mathbf{I}-\mathbf{U}(\bar{R})]\}^{-1}[\mathbf{O}^{T}(\bar{R}-h,\bar{R})\mathbf{F}(\bar{R}-h)\\&+\mathbf{O}(\bar{R},\bar{R}+h)\mathbf{F}(\bar{R}+h)].\end{aligned} \tag{C39}$$

Note that $\mathbf{U}(\bar{R})$ is a diagonal matrix and thus the inversion in Eq. (C39) is not CPU time consuming.

## APPENDIX D: $S$ PROPAGATOR

Let us assume that the local scattering matrices for the regions $(\Sigma_1,\Sigma_2)$ and $(\Sigma_2,\Sigma_3)$ are given by

$$\begin{pmatrix}R_1 & \tilde{T}_1\\ T_1 & \tilde{R}_1\end{pmatrix},\qquad \begin{pmatrix}R_2 & \tilde{T}_2\\ T_2 & \tilde{R}_2\end{pmatrix}, \tag{D1}$$

where $R$, $T$ is the reflection and transmission $S$ matrices, respectively. The full $S$ matrix for the region $(\Sigma_1,\Sigma_3)$ can then be written as

$$R=R_1+\tilde{T}_1(1-R_2\tilde{R}_1)^{-1}R_2T_1, \tag{D2}$$

$$T=T_2(1-\tilde{R}_1R_2)^{-1}T_1, \tag{D3}$$

$$\tilde{T}=\tilde{T}_1(1-R_2\tilde{R}_1)^{-1}\tilde{T}_2, \tag{D4}$$

$$\tilde{R}=\tilde{R}_2+T_2(1-\tilde{R}_1R_2)^{-1}\tilde{R}_1\tilde{T}_2, \tag{D5}$$

(see Ref. [73] for details). By applying the above relation successively to $\Sigma_1,\Sigma_2,\ldots,\Sigma_N$, we can obtain the $S$ matrix for $(\Sigma_1,\Sigma_N)$.

## APPENDIX E: STABILITY OF CTCO—ASYMPTOTIC RESULTS

Triple collision orbits (TCO) going straight into or coming out of the triple collision will do so along the Wannier orbit (WO). To evaluate the stability properties of TCO's as they approach the triple collision, we will derive first the stability of the WO near the triple collision. In the next section, we will then consider the stability of closed TCO's in general. All calculations in this Appendix will be done for fixed energy $E=-1$; the general energy dependence is obtained using the scaling relations (50). We will omit the tilde notation used in Eq. (50) in what follows.

### 1. Stability of the Wannier orbit near the triple collision

Introducing

$$\mathbf{u}=(\mathbf{r}_1-\mathbf{r}_2)/\sqrt{2};\quad \mathbf{U}=(\mathbf{r}_1+\mathbf{r}_2)/\sqrt{2}, \tag{E1}$$

the two-electron Hamiltonian (49) can be written in the form

$$H=\frac{1}{2}(\mathbf{p}^2+\mathbf{P}^2)-\frac{\sqrt{2}Z}{|\mathbf{u}-\mathbf{U}|}-\frac{\sqrt{2}Z}{|\mathbf{u}+\mathbf{U}|}+\frac{1}{\sqrt{2}u}=-1, \tag{E2}$$

where $\mathbf{p}$ and $\mathbf{P}$ are the conjugate momenta of $\mathbf{u}$ and $\mathbf{U}$, respectively. We align the collinear $eZe$ space along the $z$ axis, that is, the collinear dynamics are characterized by

$$u_1=p_1=U_1=P_1=u_2=p_2=U_2=P_2=0. \tag{E3}$$

The WO corresponds to symmetric electronic motion embeded in the $eZe$ space with $U_3=P_3=0$.

The equation of motion obtained from Eq. (E2) can be solved explicitly for $u_3(t)$ along the WO, one obtains

$$u_3=A\sin^2\frac{\xi}{2}=\frac{A}{2}(1-\cos\xi), \tag{E4}$$

$$t=\frac{A}{\sqrt{2}}\left(\frac{\xi}{2}-\sin\frac{\xi}{2}\cos\frac{\xi}{2}\right)=\frac{A}{2\sqrt{2}}(\xi-\sin\xi), \tag{E5}$$

with $A=(4Z-1)/\sqrt{2}$ and $E=-1$.

The full stability matrix describing the linearized dynamics in the vicinity of an arbitrary trajectory $\beta$ is given by the differential equation

$$\frac{d}{dt}\mathbf{M}^{(\beta)} = \mathbf{J}\mathbf{W}^{(\beta)}\mathbf{M}^{(\beta)}, \tag{E6}$$

with

$$\mathbf{W}^{(\beta)} = \left(\frac{\partial^2 H}{\partial \mathbf{X}\partial \mathbf{X}}\right)_\beta; \quad \mathbf{J} = \mathbf{I}_4 \otimes \begin{pmatrix} 0 & -1 \\ 1 & 0 \end{pmatrix}, \tag{E7}$$

$\mathbf{X} = (u_1, p_1, U_1, P_1, \ldots, u_3, p_3, U_3, P_3)$ and $\mathbf{I}_4$, the $4 \times 4$ identity matrix. The Hessian matrix $\mathbf{W}$ is block diagonal for collinear orbits and becomes diagonal on the WO having the form

$$\mathbf{W}_1^{\mathrm{WO}} = \mathbf{W}_2^{\mathrm{WO}} = \begin{pmatrix} \frac{A}{u_3^3} & 0 & 0 & 0 \\ 0 & 1 & 0 & 0 \\ 0 & 0 & \frac{2\sqrt{2}Z}{u^3} & 0 \\ 0 & 0 & 0 & 1 \end{pmatrix},$$
$$\mathbf{W}_3^{\mathrm{WO}} = \begin{pmatrix} -\frac{2A}{u^3} & 0 & 0 & 0 \\ 0 & 1 & 0 & 0 \\ 0 & 0 & -\frac{4\sqrt{2}Z}{u^3} & 0 \\ 0 & 0 & 0 & 1 \end{pmatrix}. \tag{E8}$$

Small changes in $u_i, p_i, i = 1, 2$ are related to changes in the total angular momentum and thus correspond to marginally stable degrees of freedom. Likewise, small deviations from the WO in the $u_3$ degree of freedom are related to changes along the WO and perpendicular to the energy manifold and give rise to shifts along the trajectory or in energy. The relevant degrees of freedom leading to nontrivial stability exponents can be found along the $U_i, P_i, i = 1, 2, 3$ coordinates. Small deviations from zero in $U_i, P_i, i = 1, 2$ amount to a bending-type motion which is embedded in the angular momentum $L = 0$ subspace. [In fact, these perturbations are embedded in another invariant subspace, the *Wannier ridge* space of symmetric electronic motion with constant hyperangle $\alpha = \pi/4$, see Eq. (3)]. These coordinates lie in a space perpendicular to the $eZe$ space, whereas $U_3, P_3$ represent deviations from the WO within the $eZe$ space. For the WO, the stability submatrices $\mathbf{m}^\perp, \mathbf{m}^\parallel$ in Eq. (51) are thus determined by the following differential equations

$$\frac{d}{dt}\mathbf{m}^\perp = \begin{pmatrix} 0 & 1 \\ -\frac{2\sqrt{2}Z}{u_3^3} & 0 \end{pmatrix}\mathbf{m}^\perp; \quad \frac{d}{dt}\mathbf{m}^\parallel = \begin{pmatrix} 0 & 1 \\ \frac{4\sqrt{2}Z}{u_3^3} & 0 \end{pmatrix}\mathbf{m}^\parallel. \tag{E9}$$

For fixed energy $E = -1$ and using the scaled time $\xi$ defined implicitly through Eq. (E5) with

$$\frac{d}{dt} = \frac{4}{(4Z-1)(1-\cos\xi)}\frac{d}{d\xi}, \tag{E10}$$

one obtains the second-order ordinary differential equations (ODE's) for the stability matrix elements

$$(1-\cos\xi)\frac{d^2 m_{1j}^\perp}{d\xi^2} - \sin\xi\frac{dm_{1j}^\perp}{d\xi} + \frac{4Z}{4Z-1}m_{1j}^\perp = 0, \tag{E11}$$

$$(1-\cos\xi)\frac{d^2 m_{1j}^\parallel}{d\xi^2} - \sin\xi\frac{dm_{1j}^\parallel}{d\xi} - \frac{8Z}{4Z-1}m_{1j}^\parallel = 0, \tag{E12}$$

with $j = 1, 2$. Here, we used $dm_{1j}/dt = m_{2j}$ as well as the WO solution for $u_3$ in the form (E4).

We are interested in the dynamics near the triple collision, that is, in segments of the WO with $u_3 \sim \frac{A}{4}\xi^2 \ll 1$. Linearizing Eqs. (E11) and (E12) for small $\xi$ and setting $s = \log_{10}\xi$ leads to linear ODE's with constant coefficients and independent solutions of the form

$$m_{1j}^\perp = \xi^{\lambda_\pm^\perp}; \quad m_{1j}^\parallel = \xi^{\lambda_\pm^\parallel},$$

with

$$\lambda_\pm^\perp = \frac{3}{2} \pm \frac{1}{2}\sqrt{\frac{4Z-9}{4Z-1}}, \tag{E13}$$

$$\lambda_\pm^\parallel = \frac{3}{2} \pm \frac{1}{2}\sqrt{\frac{100Z-9}{4Z-1}}. \tag{E14}$$

These exponents are stability exponents of the triple collision dynamics first studied by Siegel [77] for gravitational problems and Wannier [9] for two-electron atoms, see also Refs. [30,31,33]. Note that $\lambda_\pm^\perp$ is imaginary for $1/4 < Z < 9/4$ giving rise to stable motion in the bending degrees of freedom in this parameter regime.

We are interested in the stability properties of the WO in the vicinity of the triple collision, that is, along segments of the WO with $\xi \ll 1$ for all $\xi \in (\xi_0, \xi_1)$ between initial points $\xi_0$ and final point $\xi_1$ of the trajectory. The stability matrix $\mathbf{m}(\xi_0, \xi_1)$ is calculated with initial conditions set to $\mathbf{m}(\xi_0, \xi_0) = \mathbf{I}_2$ valid both for $\mathbf{m}^\perp$ and $\mathbf{m}^\parallel$. We obtain for the matrix elements integrated along the WO between $\xi_0$ and $\xi_1$

$$\begin{aligned} m_{11} &= \frac{1}{\lambda_+ - \lambda_-}(\lambda_- r^{\lambda_+} - \lambda_+ r^{\lambda_-}), \\ m_{12} &= \frac{4Z-1}{8}\frac{1}{\lambda_+ - \lambda_-}\xi_0^3(r^{\lambda_+} - r^{\lambda_-}), \\ m_{21} &= -\frac{8}{4Z-1}\frac{\lambda_+\lambda_-}{\lambda_+ - \lambda_-}\xi_1^{-3}(r^{\lambda_+} - r^{\lambda_-}), \\ m_{22} &= \frac{1}{\lambda_+ - \lambda_-}r^{-3}(\lambda_+ r^{\lambda_+} - \lambda_- r^{\lambda_-}), \end{aligned} \tag{E15}$$

with $r = \xi_1/\xi_0$. Equation (E15) is again valid both for $\mathbf{m}^\perp$ and $\mathbf{m}^\parallel$ after inserting the appropriate $\lambda_\pm$ coefficients.

### 2. Stability of CTCO's

Consider the segment of a CTCO $\gamma$ starting in outward direction from $\Sigma$ and finishing on $\Sigma$. We are interested in the stability matrix elements along these segments for fixed energy $E = -1$ and in the limit $R_0 \to 0$. Fixing a second surface of section at $R_1$, we write the full stability matrix along the CTCO, $\mathbf{M}_\gamma$, in the form

$$\mathbf{M}^{(\gamma)}(R_0, R_0) = \mathbf{M}^{(\gamma)}(R_0, R_1)\mathbf{M}^{(\gamma)}(R_1, R_1)\mathbf{M}^{(\gamma)}(R_1, R_0). \tag{E16}$$

Assuming $R_0 < R_1 \ll 1$, we can approximate the stability matrix of the CTCO segments close to the triple collision by the linearized dynamics along the WO, that is,

$$\mathbf{M}^{(\gamma)}(R_0, R_1) \approx \mathbf{M}^{\mathrm{WO}}(R_0, R_1),$$

with $R = u_3 \sim \xi^2$ along the WO. CTCO's are embedded in the $eZe$ space leading to a block-diagonal form of $\mathbf{M}^{(\gamma)}$ according to Eq. (E7); choosing local coordinates along the CTCO, the stability matrix can be further reduced to blocks of $(2 \times 2)$ matrices $\mathbf{m}_{\gamma}^{\perp,\parallel}$ as demonstrated for the WO in the previous section [58]. Multiplying out the matrix equation (E16) for the submatrices, one obtains (here done for the $m_{12}$ matrix element, which is of importance in the semiclassical equations in Sec. IV),

$$m_{12}^{(\gamma)} \approx m_{11}^{\downarrow} m_{11}^{\gamma} m_{12}^{\uparrow} + m_{11}^{\downarrow} m_{12}^{\gamma} m_{22}^{\uparrow} + m_{12}^{\downarrow} m_{21}^{\gamma} m_{12}^{\uparrow} + m_{12}^{\downarrow} m_{22}^{\gamma} m_{22}^{\uparrow}, \tag{E17}$$

with $m_{ij}^{\uparrow} = m^{wo}(R_1, R_0)$, $m_{ij}^{\downarrow} = m^{wo}(R_0, R_1)$, and $m_{ij}^{\gamma} = m_{ij}^{(\gamma)}(R_1, R_1)$. Evaluating the matrix elements term by term using the asymptotics of the expressions in Eq. (E15) in the limit $R_0 \to 0$ with $R_0 \sim \xi^2$, one obtains

$$m_{12}^{(\gamma),\perp} \sim R_0^{\frac{3}{2}-2\mu_{\mathrm{WR}}} \tag{E18}$$

$$m_{12}^{(\gamma),\parallel} \sim R_0^{\frac{3}{2}-2\mu_{eZe}}, \tag{E19}$$

with

$$\mu_{eZe} = \frac{1}{4}(\lambda_+^{\parallel} - \lambda_-^{\parallel}) = \frac{1}{4}\sqrt{\frac{100Z-9}{4Z-1}}, \tag{E20}$$

$$\mu_{\mathrm{WR}} = \frac{1}{4}(\lambda_+^{\perp} - \lambda_-^{\perp}) = \frac{1}{4}\sqrt{\frac{4Z-9}{4Z-1}}. \tag{E21}$$

The subscript $eZe$ and WR indicate that the instability originates from perturbations within the $eZe$ space or along the Wannier ridge. This concludes the derivation of Eqs. (52) and (53) in Sec. IV B 2 at fixed energy $E = -1$. We note that the analysis for $\mathbf{m}^{\perp}$ is valid only for $Z > 9/4$, that is, for $\mu_{\mathrm{WR}}$ being real. Also, $\lambda_+^{\perp} > \lambda_-^{\perp} > 0$ are both positive for $Z > 9/4$, the difference between competing terms is thus less pronounced for the $\mathbf{m}^{\perp}$ contributions compared to the $\mathbf{m}^{\parallel}$ contributions.


[1] G. Tanner *et al.*, Rev. Mod. Phys. **72**, 497 (2000).
[2] T. N. Rescigno, M. Baertschy, W. A. Isaacs, and C. W. McCurdy, Science **286**, 2474 (1999).
[3] M. Baertschy, T. N. Rescigno, W. A. Isaacs, X. Li, and C. W. McCurdy, Phys. Rev. A **63**, 022712 (2001).
[4] P. L. Bartlett, J. Phys. B **39**, R379 (2006).
[5] I. Bray and A. T. Stelbovics, Phys. Rev. A **46**, 6995 (1992).
[6] I. Bray, D. V. Fursa, A. Kheifets, and A. Stelbovics, J. Phys. B **35**, R117 (2002).
[7] L. Malegat, P. Selles, and A. K. Kazansky, Phys. Rev. A **60**, 3667 (1999).
[8] L. Malegat, P. Selles, and A. K. Kazansky, Phys. Rev. Lett. **85**, 4450 (2000).
[9] G. H. Wannier, Phys. Rev. **90**, 817 (1953).
[10] P. L. Bartlett and A. T. Stelbovics, Phys. Rev. Lett. **93**, 233201 (2004).
[11] C. Bouri, P. Selles, L. Malegat, and M. G. Kwato Njock, J. Electron Spectrosc. Relat. Phenom. **161**, 80 (2007).
[12] A. Huetz and J. Mazeau, Phys. Rev. Lett. **85**, 530 (2000).
[13] J. S. Briggs and V. Schmidt, J. Phys. B **33**, R1 (2000).
[14] H. Kossmann, V. Schmidt, and T. Andersen, Phys. Rev. Lett. **60**, 1266 (1988).
[15] E. Foumouo, G. L. Kamta, G. Edah, and B. Piraux, Phys. Rev. A **74**, 063409 (2006); A. Kheifets and I. A. Ivanov, J. Phys. B **39**, 1731 (2006); L. A. A. Nikolopoulus and P. Lambropoulos, *ibid.* **40**, 1347 (2007).
[16] Th. Weber *et al.*, Nature (London) **405**, 658 (2000); A. Becker, R. Dörner, and R. Moshammer, J. Phys. B **38**, S753 (2005); C. Ruiz, L. Plaja, L. Roso, and A. Becker, Phys. Rev. Lett. **96**, 053001 (2006).
[17] Y. H. Jiang, R. Puttner, R. Hentges, J. Viefhaus, M. Poiguine, U. Becker, J. M. Rost, and G. Kaindl, Phys. Rev. A **69**, 042706 (2004); Y. H. Jiang, Ph.D. thesis, Freien Universität Berlin, 2006.
[18] A. Czasch *et al.*, Phys. Scr. T **110**, 141 (2004).
[19] A. Czasch *et al.*, Phys. Rev. Lett. **95**, 243003 (2005).
[20] G. Tanner, N. N. Choi, M.-H. Lee, A. Czasch, and R. Dörner, J. Phys. B **40**, F157 (2007).
[21] R. Püttner, B. Gremaud, D. Delande, M. Domke, M. Martins, A. S. Schlachter, and G. Kaindl, Phys. Rev. Lett. **86**, 3747 (2001).
[22] Y. H. Jiang, R. Püttner, D. Delande, M. Martins, and G. Kaindl, Phys. Rev. A **78**, 021401(R) (2008).
[23] A. Bürgers, D. Wintgen, and J.-M. Rost, J. Phys. B **28**, 3163 (1995).
[24] J. Eiglsperger and J. Madroñero, Phys. Rev. A **80**, 022512 (2009).
[25] H. W. van der Hart and C. H. Greene, Phys. Rev. A **66**, 022710 (2002).
[26] T. Schneider, C.-N. Liu, and J.-M. Rost, Phys Rev A **65**, 042715 (2002).
[27] A.-T. Le, T. Morishita, X.-M. Tong, and C. D. Lin, Phys. Rev. A **72**, 032511 (2005).
[28] M. M. Sano, Phys. Rev. E **75**, 026203 (2007).
[29] M.-H. Lee, G. Tanner, and N. N. Choi, Phys. Rev. E **71**, 056208 (2005).
[30] N. N. Choi, M.-H. Lee, and G. Tanner, Phys. Rev. Lett. **93**, 054302 (2004).
[31] Z.-Q. Bai, Y. Gu, and J. M. Yuan, Physica D **118**, 17 (1998).
[32] M. M. Sano, J. Phys. A **37**, 803 (2004).
[33] C. W. Byun, N. N. Choi, M.H. Lee, and G. Tanner, Phys. Rev. Lett. **98**, 113001 (2007).
[34] F. Mrugała and D. Secrest, J. Chem. Phys. **78**, 5954 (1983).
[35] F. Mrugała and D. Secrest, J. Chem. Phys. **79**, 5960 (1983).
[36] F. Mrugała, Int. Rev. Phys. Chem. **12**, 1 (1993).
[37] E. B. Bogomolny, Zh. Eksp. Teor. Fiz. **96**, 487 (1989) [Sov. Phys. JETP **69**, 275 (1989)].
[38] M. L. Du and J. B. Delos, Phys. Rev. A **38**, 1896 (1988).
[39] T. Prosen, J. Phys. A **28**, 4133 (1995).
[40] C. Rouvinez and U. Smilansky, J. Phys. A **28**, 77 (1995).
[41] U. Fano, Rep. Prog. Phys. **46**, 97 (1983).
[42] C. D. Lin, Phys. Rep. **257**, 1 (1995).

[43] E. B. Bogomolny, Nonlinearity **5**, 805 (1992).
[44] E. Doron and U. Smilansky, Nonlinearity **5**, 1055 (1992).
[45] B. E. Granger and C. H. Greene, Phys. Rev. A **62**, 012511 (2000).
[46] D. Delande, K. T. Taylor, M. H. Halley, T. van der Veldt, and W. Hogervorst, J. Phys. B **27**, 2771 (1994).
[47] P. A. Dando, T. S. Monteiro, D. Delande, and K. T. Taylor, Phys. Rev. Lett. **74**, 1099 (1995); Phys. Rev. A **54**, 127 (1996).
[48] T. Bartsch, J. Main, and G. Wunner, Phys. Rev. A **67**, 063411 (2003).
[49] J. A. Shaw and F. Robicheaux, Phys. Rev. A **58**, 3561 (1998).
[50] B. R. Johnson, J. Comput. Phys. **13**, 445 (1973).
[51] M. Baer, G. Drolshagen, and J. P. Toennies, J. Chem. Phys. **73**, 1690 (1980).
[52] F. Mrugała and J. Römelt, Chem. Phys. **118**, 295 (1987).
[53] O. I. Tolstikhin, S. Watanabe, and M. Matsuzawa, J. Phys. B **29**, L389 (1996).
[54] D. Kato and S. Watanabe, Phys. Rev. A **56**, 3687 (1997); F. D. Colavecchia, F. Mrugała, G. A. Parker, and R. T. Pack, J. Chem. Phys. **118**, 10387 (2003); C.-N. Liu, A.-T. Le, T. Morishita, B. D. Esry, and C. D. Lin, Phys. Rev. A **67**, 052705 (2003); X. Guan, X.-M. Tong and S. I. Chu, *ibid.* **73**, 023403 (2006); J. Blandon, V. Kokoouline, and F. Masnou-Seeuws, *ibid.* **75**, 042508 (2007).
[55] B. Hüpper, J. Main, and G. Wunner, Phys. Rev. Lett. **74**, 2650 (1995); Phys. Rev. A **53**, 744 (1996).
[56] M. Keeler and T. J. Morgan, Phys. Rev. Lett. **80**, 5726 (1998).
[57] W. Huang and T. J. Morgan, Phys. Rev. A **65**, 033409 (2002).
[58] K. Richter, G. Tanner, and D. Wintgen, Phys. Rev. A **48**, 4182 (1993).
[59] M.-H. Lee, N. N. Choi, and G. Tanner, Phys. Rev. E **72**, 066215 (2005).
[60] J.-M. Rost, Phys. Rep. **297**, 271 (1998).
[61] M. C. Gutzwiller, *Chaos in Classical and Quantum Mechanics* (Springer, New York, 1990).
[62] K. Richter and D. Wintgen, J. Phys. B **23**, L197 (1990).
[63] R. McGehee, Inventiones Mathematicae **27**, 191 (1974).
[64] B. Eckhardt and D. Wintgen, J. Phys. A **24**, 4335 (1991).
[65] A. Temkin and Y. Hahn, Phys. Rev. A **9**, 708 (1974).
[66] G. S. Ezra, K. Richter, G. Tanner, and D. Wintgen, J. Phys. B **24**, L413 (1991).
[67] D. Wintgen, K. Richter, and G. Tanner, CHAOS **2**, 19 (1992).
[68] H. Bachau *et al.*, Rep. Prog. Phys. **64**, 1815 (2001).
[69] B. R. Johnson, J. Chem. Phys. **69**, 4678 (1978).
[70] A. E. Thornley and J. M. Hutson, J. Chem. Phys. **101**, 5578 (1994).
[71] D. E. Manolopoulos, J. Chem. Phys. **85**, 6425 (1986).
[72] R. T. Pack and G. A. Parker, J. Chem. Phys. **87**, 3888 (1987).
[73] R. O. Vallejos and A. M. Ozorio de Almeida, Ann. Phys. (NY) **278**, 86 (1999).
[74] R. Püttner (private communication).
[75] D. Delande (private communication).
[76] J. Madroñero (private communication).
[77] C. L. Siegel, Ann. Math. **42**, 127 (1941); J. Waldvogel, Lect. Notes Phys. **590**, 81 (2002).